MONOLITHIC INTEGRATION
OF GALLIUM ARSENIDE OPTOELECTRONIC DEVICES

Thesis by

Israel Ury

In Partial Fulfillment of the Requirements

for the degree of

Doctor of Philosophy

California Institute of Technology

Pasadena, California

1980

(Submitted April 28, 1980)

To My Fiancée

and To Our Parents

ACKNOWLEDGMENTS

I would like to express my appreciation and thanks to my advisor, Professor Amnon Yariv, for his guidance throughout the course of this work. I have profited greatly from the experience gained working under his supervision.

I am especially indebted to Dr. Shlomo Margalit for having suggested to me much of the work contained in this thesis. His constant willingness to discuss new ideas was of particular value. I would like to thank Dr. Chien-Ping Lee for his collaboration on some of the work described in this thesis and for instructing me in the art of epitaxial crystal growth. Thanks are also due to the other members of the semiconductor quantum electronics group with whom I have worked these past years: Mr. Moshe Yust, Dr. Nadav Bar-Chaim, Dr. Hossein Izadpanah, Mr. Pei-Chuang Chen, Mr. Daniel Wilt, Mr. Joseph Katz, Mr. Kam Lau, and Mr. Paul Yu.

I am grateful to Mr. Desmond Armstrong and Mr. Lawrence Begay for constructing some of the experimental apparatus used in this work. I am also grateful to Mrs. Ruth Stratton for typing this thesis in such an expert fashion.

I am thankful for the financial support received from the California Institute of Technology, the National Science Foundation, and the Office of Naval Research.

My deepest appreciation goes to my parents for their support and encouragement of my undertaking this work, and to my fiancee, Miss Gittie Zelcer for providing me with the motivation to complete this work.

ABSTRACT

The optical properties of GaAs make it a very useful material for the fabrication of optical emitters and detectors. GaAs also possesses electronic properties which permit the fabrication of high speed electronic devices which are superior to conventional silicon devices. This thesis describes three examples of the *monolithic integration* of optical and electronic devices on semi-insulating GaAs substrates.

In the first example, an injection laser was integrated with a Gunn oscillator to yield a high frequency modulated optical source. In the second example, an injection laser was integrated with a metal semiconductor field effect transistor (MESFET). The transistor was used to modulate the current through the laser. In the third example, an integrated optical repeater was demonstrated which consisted of a MESFET optical detector, a current source, a transistor driver, and an injection laser all fabricated on a single chip. The repeater displayed an optical gain of 10 dB.

In order to facilitate the fabrication of more complex integrated optoelectronic circuits, a method was sought to form a laser cavity which did not occupy the entire width of a chip. The result was the demonstration of whispering gallery lasers which take the shape of quarter and half rings. The performance of the curved lasers was reduced from that of the straight lasers due to optical scattering at imperfections along the curve. A general theory is developed which describes mode conversion in perturbed dielectric resonators. This

theory is applied to the case of the whispering gallery laser and its predictions are compared with experiment.

TABLE OF CONTENTS

CHAPTER I

INTRODUCTION

Over the past half century the world has been experiencing what has become known as the electronic revolution. At the present time it is difficult to even imagine what life would be like without digital computers or without the electronic media. Most recently, electronics has pervaded our society even more heavily, in large measure due to the proliferation of silicon integrated circuits. It now appears that in certain applications where speed is of utmost importance, or where optical interfacing is desired, GaAs and its related compounds may supersede silicon.

The economic factors which have led to the tremendous growth of the multi-billion dollar silicon-based electronics industry are: 1) the low cost of materials which go into a single chip, and 2) the high volume planar fabrication techniques which allow millions of transistors to be literally "printed up" simultaneously on a single silicon wafer. The "printing" process is conventionally done photolithographically, although other more advanced methods of feature delineation such as electron beam and x-ray exposure techniques are being developed to fabricate even more complex and dense electronic circuits. Two of the more important physical properties of silicon which make it such an attractive electronic material are: 1) the ease with which it can be doped n- or p-type, and 2) the durability and simplicity of growth of its native oxide, SiO_2.

GaAs is potentially superior to silicon as a material for the fabrication of electronic devices because of its higher electron mobility. The approximately ten times larger electron mobility means that faster and smaller transistors can be built in GaAs. So far this advantage of GaAs over silicon has manifested itself chiefly in the commercial availability of GaAs transistors which are usable at frequencies of tens of GHz.[1] GaAs-based technology has also been making inroads as a competitor to silicon-based technology, not only in the area of discrete high frequency devices, but also in the realm of very high speed integrated circuits.[2]

Over the past ten years or so, interest has been turning toward optics to provide solutions to some of the problems encountered in electronics, particularly in the area of high speed, high volume storage and dissemination of information. Some areas of particular interest are: 1) high speed communication over low cost, low loss, interference free optical fibers, 2) high density optical disc recording of digital data, video, or audio information, and 3) document generation applications such as printers and copiers. To achieve these ends, the optical properties of semiconductors have been exploited for the generation, processing, and detection of light. Silicon can be used as an efficient optical detector of photons which are more energetic than its bandgap (corresponding to a wavelength of $\sim$1 μm). Silicon cannot be used for the generation of light, however, because its bandgap is indirect. The semiconductors which have received the most attention for use as optical sources have been the III-V binary, ternary, and quaternary compounds,

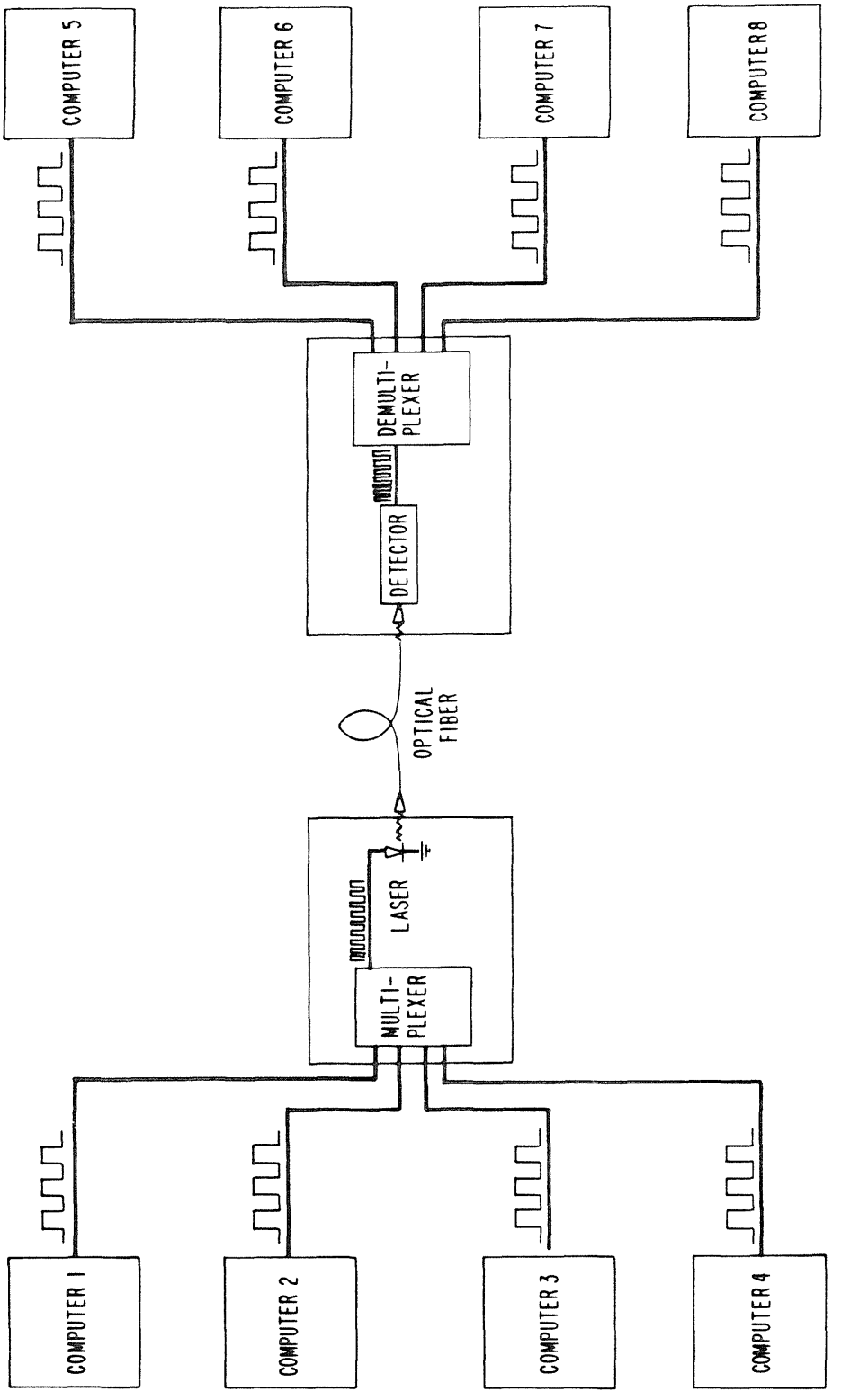

Fig. 1.1 An example of how a monolithic optoelectronic multiplexer and demultiplexer can be applied to computer networking

GaAs, GaAlAs, and GaInAsP. Of these, the most highly developed has been the GaAs/GaAlAs system.

In all the applications which have been mentioned, the optical components are actually part of a larger electronic system. In all these systems there is a need to transform information back and forth from an optical to an electronic form. Since GaAs is a semiconductor which has almost ideal electronic and optical properties, it is possible to integrate these functions on a single chip, as first suggested by Yariv.[3] This possibility provided the motivation for the work described in this thesis.

An example of the kind of systems which can benefit from monolithic optoelectronic integration are the multiplexer and demultiplexer shown in Fig. 1.1. Computers one through four are interfaced to computers five through eight by one chip which converts the low bit rate signals to a single high bit rate signal, which is converted to an optical signal, and by a second chip which detects the optical signal, and electronically separates out the individual electrical signals. It is to be noted that all the high speed electronic circuitry is on the chip, obviating any need for high speed electrical interconnections. Monolithic optoelectronic integration also has the potential of improving the reliability of a system while simultaneously decreasing its cost.

In the succeeding chapters a description will be given of the progress to date towards the realization of several integrated optoelectronic circuits. All of the circuits to be described make use of double heterostructure injection lasers. For a description of the basic physics and the common means of fabricating diode lasers, the reader is referred

to any of a number of standard texts [4,5,6,7].

REFERENCES FOR CHAPTER I

1. C. A. Liechti, "Microwave Field-Effect Transistors--1976," IEEE Trans. Microwave Theory and Techniques MTT-24, 279 (1976).
2. C. A. Liechti, "GaAs FET Logic," Proc. 6th International Symp. on GaAs and Related Compounds, Pt. I, Edinburgh, Scotland, 1976, Inst. Phys., London (1977).
3. A. Yariv, "Active Integrated Optics," Proc. Esfahan Symposium on Fundamental and Applied Laser Physics, M. S. Feld, A. Javan, and N. A. Kurnit, eds., Wiley-Interscience, New York (1973).
4. A. Yariv, Quantum Electronics, 2nd edition, John Wiley and Sons, Inc., New York (1975).
5. A. Yariv, Introduction to Optical Electronics, 2nd edition, Holt, Rinehart, and Winston, New York (1976).
6. H. C. Casey and M. B. Panish, Heterostructure Lasers: Part A, Fundamental Principles; Part B, Materials and Operating Characteristics, Academic Press, New York (1978).
7. H. Kressel and J. K. Butler, Semiconductor Lasers and Heterojunction LEDs, Academic Press, New York (1977).

CHAPTER II

LASERS ON SEMI-INSULATING SUBSTRATES

II.1 Introduction

The construction of monolithic integrated optoelectronic circuits is greatly facilitated by the use of insulating substrates to provide electrical isolation between the various devices on the chip. A fortunate set of circumstances exists for GaAs-based technology in that chromium- and oxygen-doped semi-insulating (SI) substrates have been commercially available for some time. Since electronic integrated circuits have already been fabricated on SI GaAs substrates,[1,2] it became necessary to focus attention on developing optical devices which are constructed on SI substrates. This chapter will describe the fabrication on SI GaAs substrates of one of the key components in high speed optical systems, the injection laser.

The pioneering work in the fabrication of lasers on SI substrates was performed by Lee, Margalit, and Yariv with the development of the crowding effect laser.[3] Other laser structures which will be described in this chapter include the high- and low-mesa T-laser, and the laterally diffused junction laser.

II.2 The Crowding Effect Laser and the T-Laser

The first laser to be fabricated on a SI GaAs substrate was the crowding effect laser (CEL).[3] The principle of operation of this laser can be understood by referring to Fig. 2.1. Lasing action occurs under conditions of forward bias in the thin GaAs active layer which is located at the p-n junction. The larger bandgap, lower refractive index

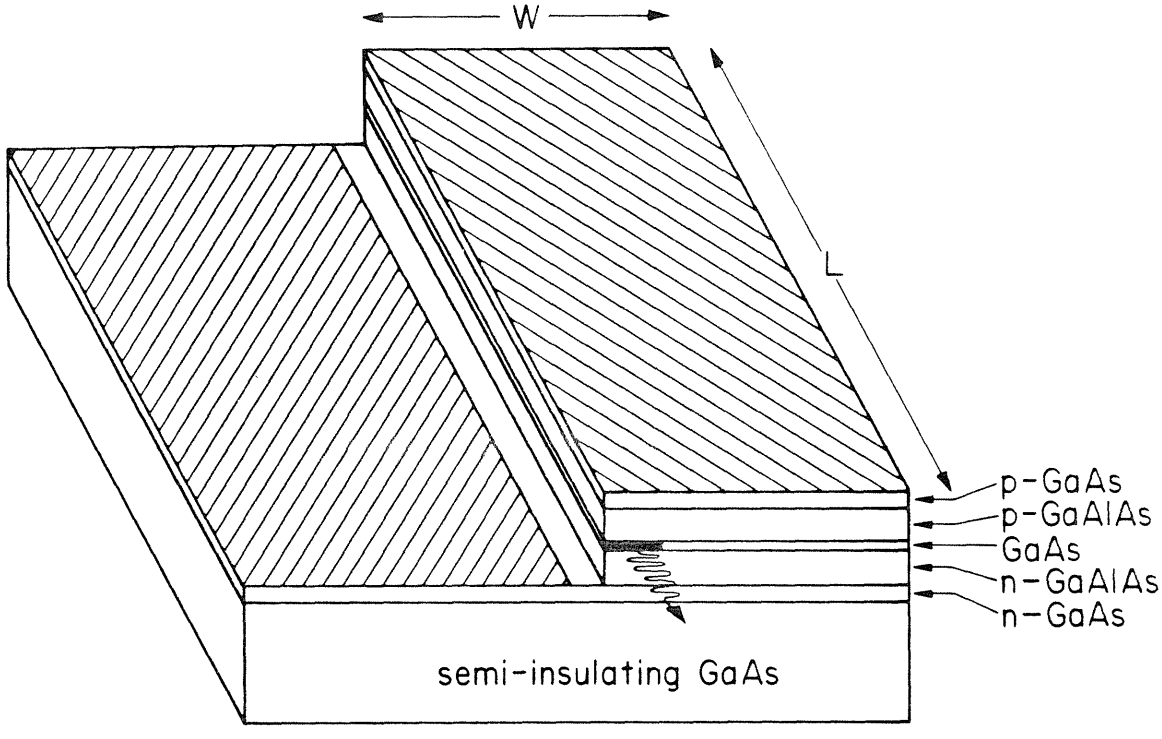

Fig. 2.1 A schematic illustration of a crowding effect laser

GaAlAs cladding layers serve to confine both the injected carriers and the optical field. Optical feedback is provided in the conventional manner by the reflection provided by the cleaved end facets. For purposes of illustration, the p-layers are shown in the figure to be situated above the n-layers, although devices fabricated in both polarities have been shown to operate.

When the diode is forward biased, current flows down through the mesa across the junction, through the lower n-layer, and into the cathode contact. A lateral voltage drop is induced in the lower n-layers owing to their resistivities. This restricts injection along the p-n junction to the immediate vicinity of the mesa edge. The region possessing optical gain therefore lies only along a very narrow stripe whose width is typically on the order of $\sim$ 10 μm. When the diode is lasing, the optical mode which propagates through the gain region is bounded on one side by the refractive index step at the mesa edge, and on the other side by the loss region in the unpumped portion of the active layer. For a detailed analysis of the optical properties of the crowding effect laser, one is referred to the work of Lee.[4,5]

To perform an analysis of the distribution of injected current in a CEL which includes the effects of contact resistance and p-layer resistance, we form an equivalent circuit as shown in Fig. 2.2. The parameters L and W are as defined by Fig. 2.1; R_n and R_p are the sheet resistances ($\Omega/\square$) of the n- and p-GaAs layers, respectively, and R_c is the p-type contact resistance (Ω-cm^2). The lateral current which flows in the n-layer is denoted by I(x), and the injected current density

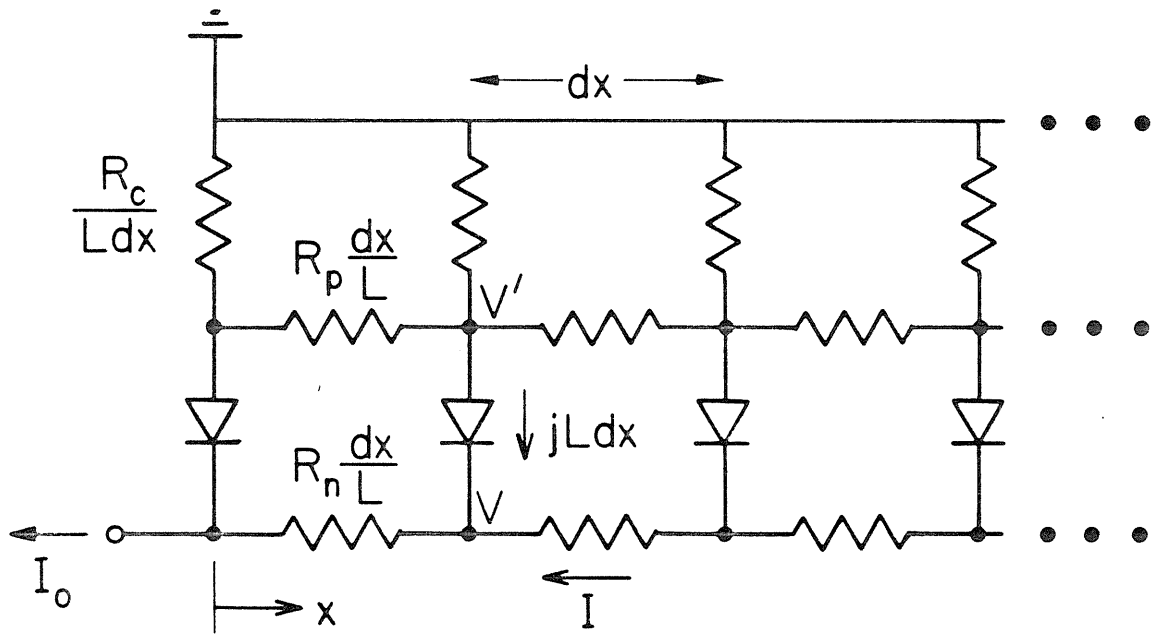

Fig. 2.2 The equivalent circuit of a crowding effect laser

across the junction is denoted by $j(x)$. The p-contact is assumed to be grounded, the potential in the n-layer is given by $V(x)$, and the potential in the p-layer is given by $V'(x)$. From the principle of conservation of current, we have

$$\frac{dI}{dx} = -j(x)\, L \tag{2.1}$$

and from Ohm's law we have that

$$\frac{dV}{dx} = \frac{I}{L} R_n \tag{2.2}$$

Considering current conservation in the p-layer, and taking the limit of dx infinitesimal, we obtain

$$j = -\frac{V'}{R_c} + \frac{1}{R_p}\frac{d^2V'}{dx^2} \tag{2.3}$$

Furthermore, let us take the injected current density to be given by[6]

$$j = j_s\, e^{\frac{q}{nkT}(V' - V)} \tag{2.4}$$

where j_s is the reverse saturation current density, n is a parameter whose value is ~ 2, and where a factor of -1 has been neglected in favor of the exponential factor whose value can always be taken to be large under forward bias. From the last equation we obtain

$$V' = V + \frac{nkT}{q} \ln\left(\frac{j}{j_s}\right) \tag{2.5}$$

By differentiating equation (2.3) with respect to x, and using equations (2.1), (2.2), and (2.5), the desired differential equation is obtained, which is of order four

$$\left(1 + \frac{R_n}{R_p}\right) \frac{d^2}{dx^2}\left(\frac{I}{L}\right) - \frac{R_n}{R_c}\left(\frac{I}{L}\right) - \frac{nkT}{qR_c} \frac{d}{dx}\left\{\ell n\left[- \frac{d}{dx}\left(\frac{I}{L}\right)\right]\right\}$$

$$+ \frac{nkT}{qR_p} \frac{d^3}{dx^3}\left\{\ell n\left[- \frac{d}{dx}\left(\frac{I}{L}\right)\right]\right\} = 0 \qquad (2.6)$$

The desired boundary conditions are that the current I(x) be known at x = 0, that it be zero at x = w, and that there should be no lateral current in the p-layer at either boundary, which we express as

$$I(0) = I_o$$

$$I(w) = 0$$

$$\frac{d^2}{dx^2}\left(\frac{I}{L}\right)\Big|_{x=0} = \frac{qR_n}{nkT}\left(\frac{I_o}{L}\right) \frac{d}{dx}\left(\frac{I}{L}\right)\Big|_{x=0} \qquad (2.7)$$

$$\frac{d^2}{dx^2}\left(\frac{I}{L}\right)\Big|_{x=w} = 0$$

It is useful to solve equation (2.6) for the case $R_c = 0$. (The result is the same if we choose $R_p = 0$.) In this case, all the current crowding is due to the resistivity of the n-layer. In this limit equation (2.6) becomes

$$\left(\frac{I}{L}\right) \frac{d}{dx}\left(\frac{I}{L}\right) = - \frac{nkT}{qR_n} \frac{d^2}{dx^2}\left(\frac{I}{L}\right) \qquad (2.8)$$

The form of the solution of equation (2.8) depends on whether we choose w to be finite or not. If w is infinite, the solution is

$$I(x) = \frac{I_o}{1 + \frac{x}{x_o}}$$

and

$$j(x) = \frac{\frac{I_o}{Lx_o}}{(1 + \frac{x}{x_o})^2} \tag{2.9}$$

where we have defined a crowding distance to be

$$x_o = \frac{2nkTL}{qR_n I_o} \tag{2.10}$$

As an example, if we choose $R_n = 100\,\Omega/\square$, $L = 300\ \mu m$, $n = 2$, and $I_o = 100$ mA, we obtain $x_o = 3.1\ \mu m$.

In the case of a finite value of w, the solution to equation (2.8) becomes

$$I(x) = I_o(\frac{x_o L j(0)}{I_o} - 1)^{1/2} \tan[(\frac{x_o L j(0)}{I_o} - 1)^{1/2} (\frac{w-x}{x_o})] \tag{2.11}$$

and

$$j(x) = (j(0) - \frac{I_o}{Lx_o}) \sec^2[(\frac{x_o L j(0)}{I_o} - 1)^{1/2} (\frac{w-x}{x_o})] \tag{2.12}$$

The value of j(0) can be determined by evaluating equation (2.11) at x = 0. The result is the implicit relationship,

$$(\frac{j(0)}{I_o/Lw} \frac{x_o}{w} - 1)^{-1/2} = \tan[(\frac{j(0)}{I_o/Lw} \frac{x_o}{w} - 1)^{1/2} \frac{w}{x_o}] \tag{2.13}$$

whose solution is plotted in Fig. 2.3. If we investigate the solution of equation (2.13) in the limit of large and small w, we obtain,

$$\begin{aligned} j(0) &= I_o/Lw \ , \qquad w \ll x_o \\ j(0) &= I_o/Lx_o \ , \qquad w \gg x_o \end{aligned} \tag{2.14}$$

These relations indicate the expected result, that for mesa widths much

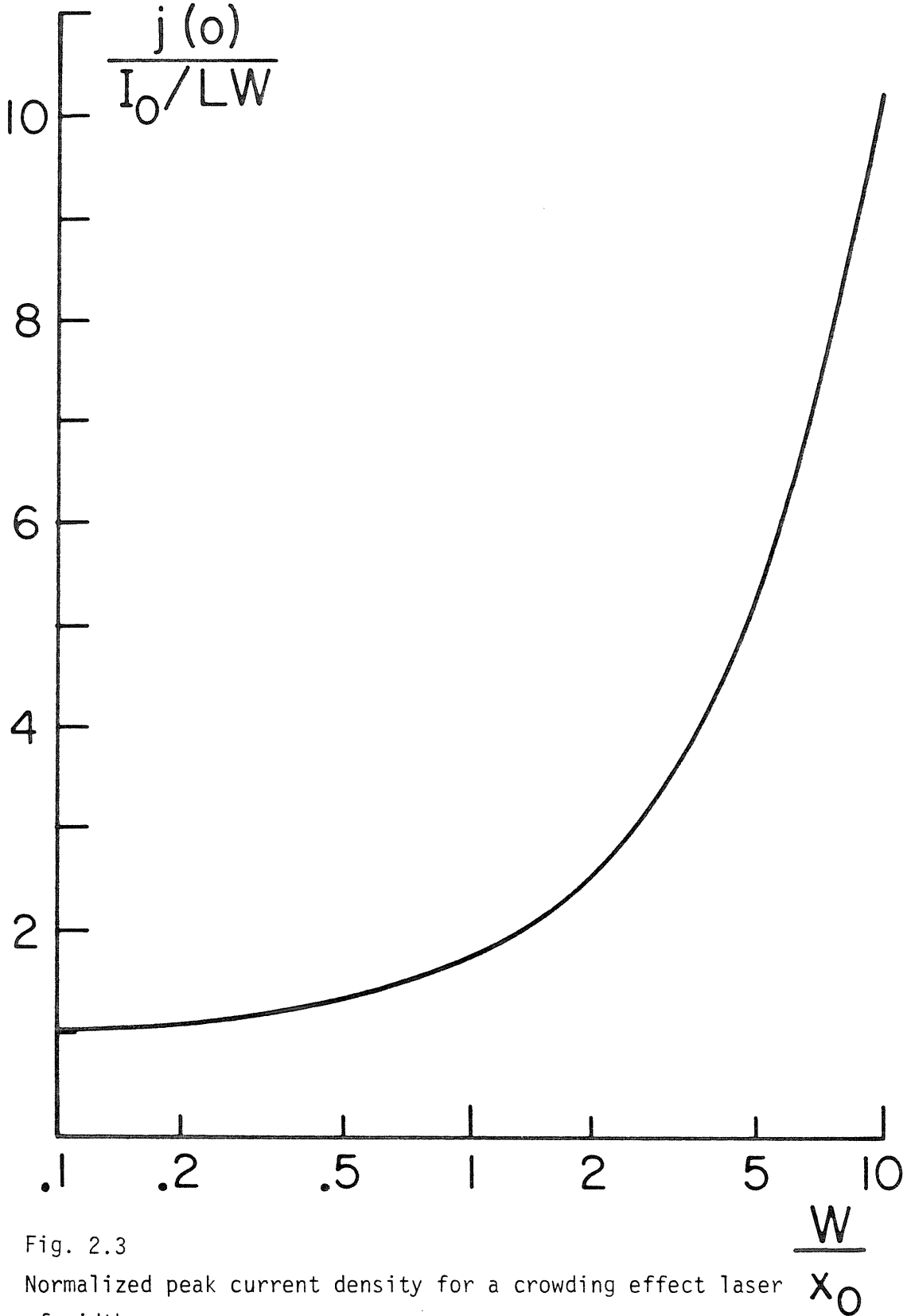

Fig. 2.3
Normalized peak current density for a crowding effect laser of width w

larger than the crowding distance, the device behaves as the infinitely wide CEL, and for mesa widths much smaller than the crowding distance, the effects of crowding can be neglected.

The above solutions to equation (2.6) which govern the crowding of injected current were obtained assuming $R_c = 0$. The effect of a finite value of contact resistance is to smooth out the distribution of injected current density in the mesa, and hence to increase the effective crowding distance. Thus the smallest value of R_c should be striven for in fabricating a CEL to achieve the most effective crowding. The effect of the contact resistance on crowding can be reduced by choosing values of the doping and thickness of the p-layers such that R_p is small. A highly conducting p-layer "shorts out" the p-side of the junction and thus eliminates the effect of the contact resistance.

The effect of contact resistance is observed experimentally by a widening of the spontaneous emission region near the mesa edge over what would be expected if contact resistance could be neglected. Since the fundamental optical mode of a CEL can be very narrow, as small as ~ 5 μm wide,[7] the excess current injected into the region not occupied by the optical mode is wasted.

A simple solution to the problem of current spreading is to reduce the width of the mesa. A bonus is incurred by narrowing the width of the mesa owing to the formation of a real index waveguide which, because it is absent in the wide CEL, leads to asymmetric output beams. This is the basis for the idea of the T-laser shown in Fig. 2.4.

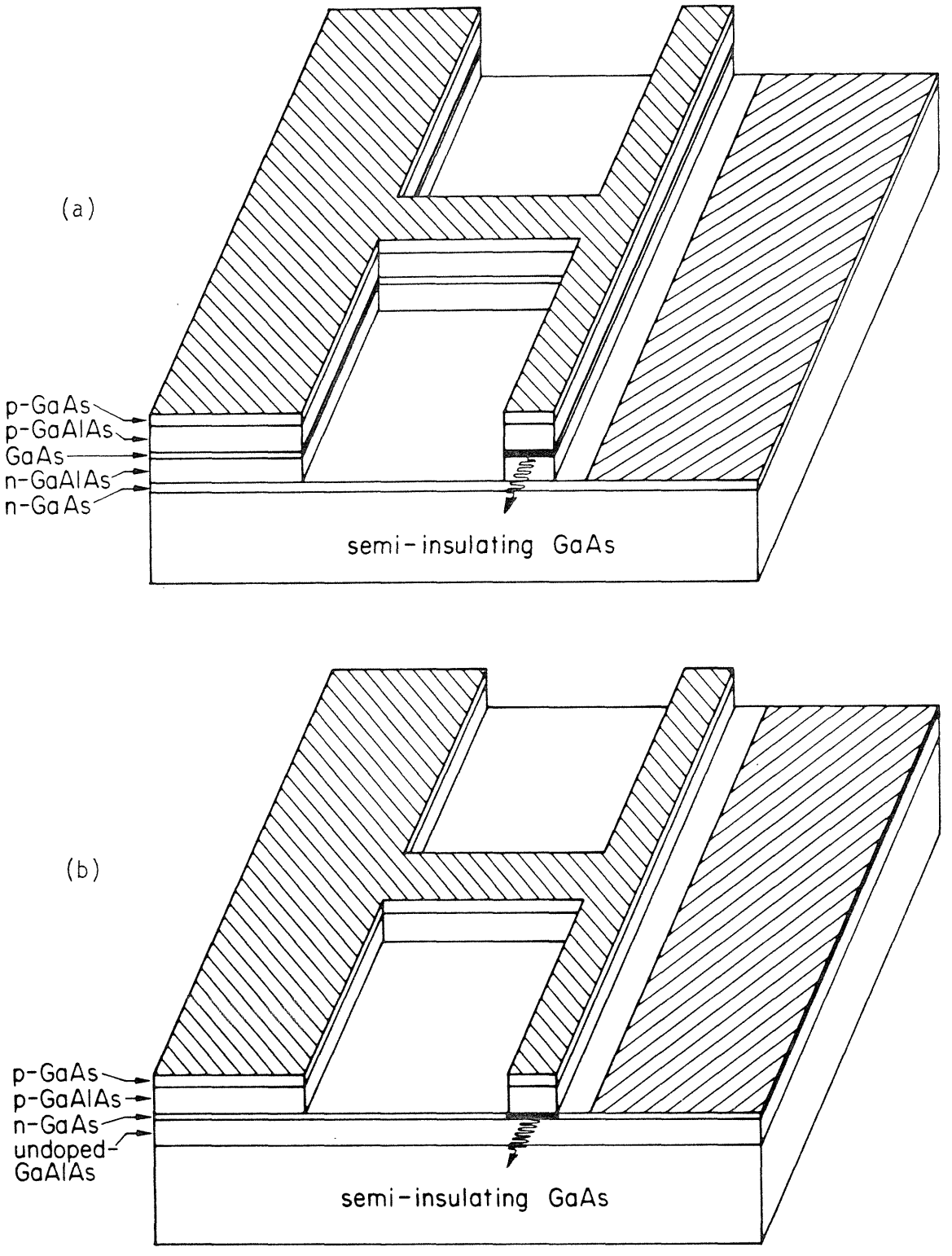

Fig. 2.4 A schematic illustration of (a) a high mesa T-laser, and (b) a low mesa T-laser

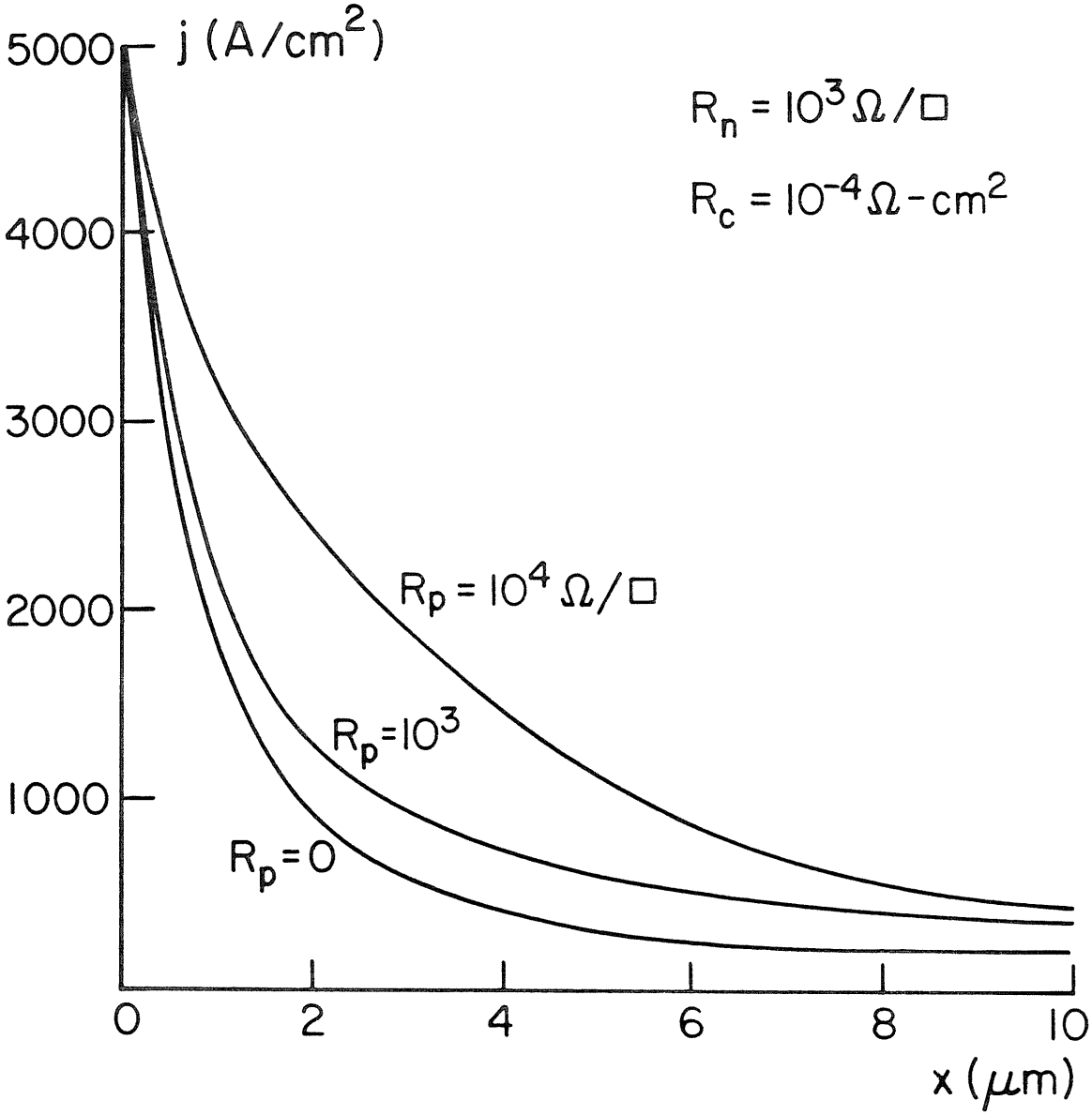

Fig. 2.5 The effect of p-layer resistance on a crowding effect laser for w = 10 μm

The distribution of injected current density in a 10 μm wide mesa is shown in Fig. 2.5 for various values of the sheet resistances of the p-layer. The curves were obtained by solving equation (2.6) numerically on a digital computer (Apple II) for a device having a crowding distance x_0 = 1.3 μm.

The T-laser is a practical design which allows for the contacting of a very narrow mesa. Schematic illustrations of two types of T-laser, the high mesa T and the low mesa T, are shown in Fig. 2.4. The T-laser gets its name from the figure described by the junction of the contact arm and the laser mesa. The lasers are similar to the high mesa and low mesa lasers on n^+-GaAs substrates,[8] but with lateral rather than vertical contacts.

Current in the devices passes from the Au-Zn p-type contact pad, along the connecting arm, down through the laser mesa, and into the n-type Au-Ge contact pad. Leakage currents associated with the large area p-n junction which resides under the contact pad and the connecting arm to the T are kept down by the sheet resistance of the n-layers. The isolation resistance in the high mesa T-laser is provided by the resistivity of the bottom n-GaAlAs and n-GaAs layers, while in the low mesa T-laser it is provided by the resistivity of only the active layer. The series resistance which is thus introduced effectively cuts off current to the parasitic diode.

Performances of the two types of structures were comparable. Room temperature pulsed threshold currents for the device were found to lie in the 100-200 mA range. The lowest threshold current obtained was 87 mA for a 5 μm by 300 μm low mesa T-laser.[9] The laser emission spectrum for

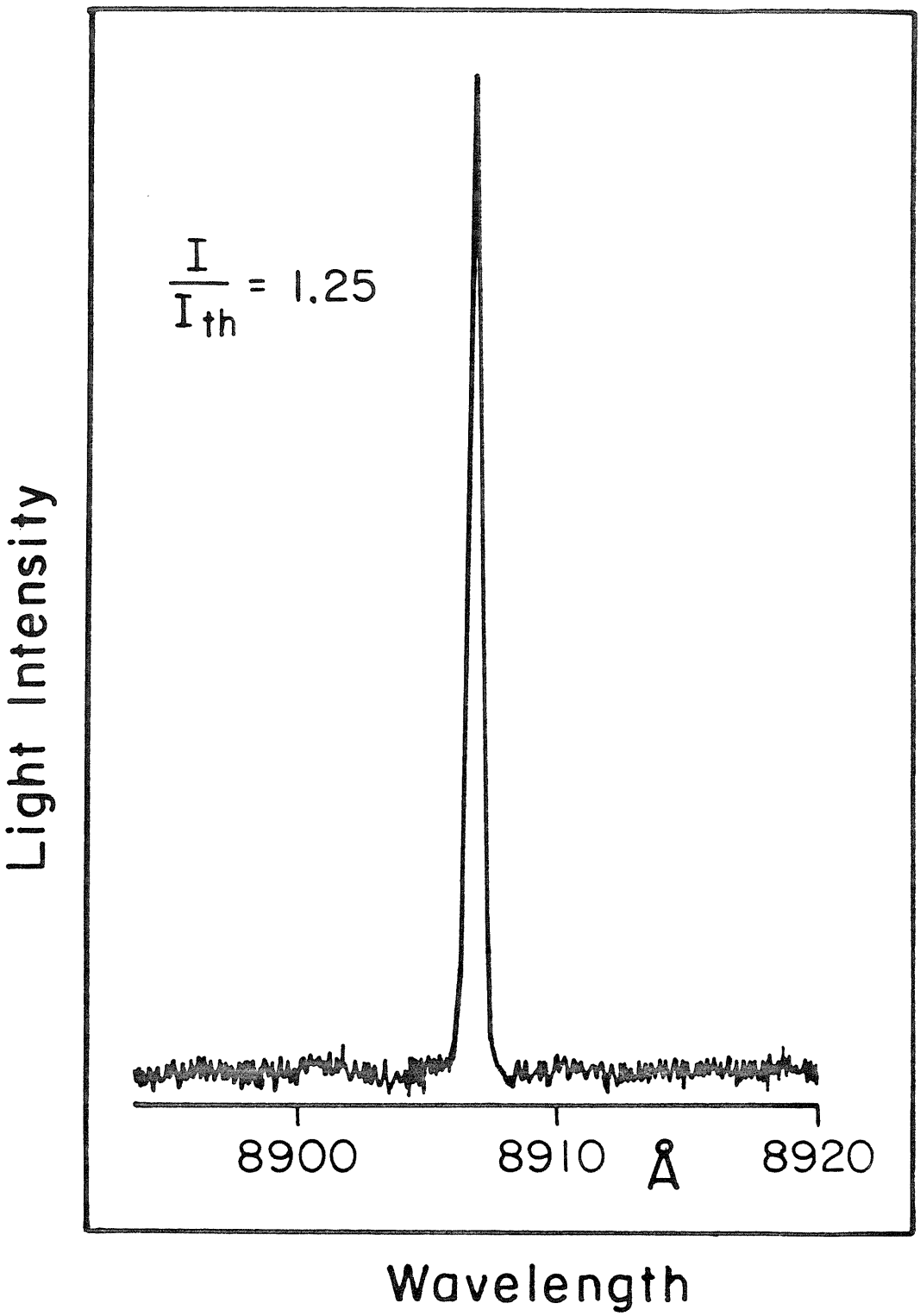

Fig. 2.6 Emission spectrum of a low mesa T-laser

a low mesa T-laser is shown in Fig. 2.6. Single longitudinal mode behavior was observed for currents up to 25% above threshold. At higher levels of excitation, two longitudinal modes were characteristically observed. Details of T-laser fabrication will be given in Section III.3.

II.3 The Laterally Diffused Junction Laser

Both the crowding effect laser and the T-laser have the advantage of being fairly simple to fabricate; however, there are several factors which degrade their performance and render them commercially unattractive. Both the CEL and the T-laser suffer from the presence of an etched interface adjacent to the lasing region. This causes carrier loss due to surface recombination, and also forms a source of possible defect generation. The CEL generally emits a beam which exits the mirror facet at an angle to the propagation direction of the optical waveguide. The T-laser has a symmetrical waveguide, but the large difference in refractive index inside and outside the waveguide leads to multi-transverse mode oscillations.

A structure which is not plagued by any of the above problems is the laterally diffused junction (LDJ) laser, which is also known as the transverse junction stripe (TJS) laser. The structure of the LDJ laser is shown in Fig. 2.7. The lateral p-n junction is formed by a deep Zn diffusion. Virtually all the current which crosses the junction does so only through the active layer. This is because the turn-on voltage for the parasitic diodes in the GaAlAs cladding layers is higher due to their larger band gap.

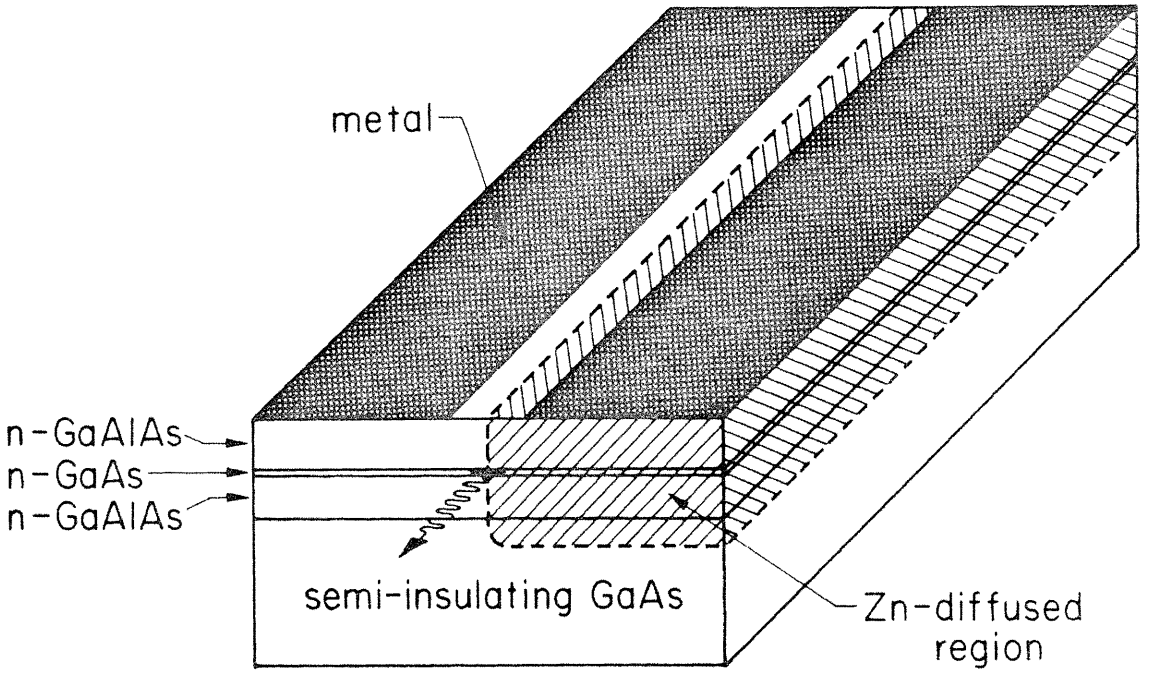

Fig. 2.7 A schematic drawing of a laterally diffused junction laser

In the original implementation of this structure on a semi-insulating substrate[10] an additional top layer of GaAs was used as a diffusion mask and subsequently removed. Single longitudinal mode behavior and threshold currents as low as 35 mA for a $\sim$300 μm long device were obtained. In subsequent commercial development of this structure,[11] Si_3N_4 was used as a diffusion mask, and an additional top n^+-GaAs layer was included to reduce the contact resistance. Threshold currents as low as 15 mA have been obtained for this structure, and lifetimes of a million hours[12] are projected.

REFERENCES FOR CHAPTER II

1. R. Van Tuyl and C. Liechti, "High-Speed Integrated Logic with GaAs MESFETs," IEEE J. Solid State Circuits SC-9, 269 (1974).
2. C. A. Liechti, "GaAs FET Logic," Proc. 6th International Symp. on GaAs and Related Compounds, Pt. I, Edinburgh, Scotland, 1976, Inst. Phys., London (1977).
3. C. P. Lee, S. Margalit, and A. Yariv, "Double-Heterostructure GaAs-GaAlAs Injection Lasers on Semi-Insulating Substrates Using Carrier Crowding," Appl. Phys. Lett. 32, 410 (1978).
4. C. P. Lee, S. Margalit, and A. Yariv, "Waveguiding in an Exponentially Decaying Gain Medium," Optics Commun. 25, 1 (1978).
5. C. P. Lee,"New Optoelectronic Devices Using GaAs-GaAlAs Epitaxy," Doctoral Thesis, California Institute of Technology, Pasadena, California (1978).
6. H. C. Casey and M. B. Panish, Heterostructure Lasers: Part B, Materials and Operating Characteristics, Academic Press, New York (1978).
7. C. P. Lee, S. Margalit, I. Ury, and A. Yariv, "Integration of an Injection Laser with a Gunn Oscillator on a Semi-Insulating GaAs Substrate," Appl. Phys. Lett. 32, 806 (1978).
8. T. Tsukada, R. Ito, H. Nahashima, and O. Nakada, "Mesa-Stripe-Geometry Double-Heterostructure Injection Lasers," IEEE J. Quantum Electronics QE-9, 356 (1973).
9. I. Ury, S. Margalit, M. Yust, and A. Yariv, "Monolithic Integration of an Injection Laser and a Metal Semiconductor Field Effect Transistor," Appl. Phys. Lett. 34, 430 (1979).

10. C. P. Lee, S. Margalit, I. Ury, and A. Yariv, "GaAs-GaAlAs Injection Lasers on Semi-Insulating Substrates Using Laterally Diffused Junctions," Appl. Phys. Lett. 32, 410 (1978).

11. H. Kumabe, T. Tanaka, H. Namizaki, M. Ishii, and W. Susaki, "High Temperature Single-Mode CW Operation with a Junction-Up TJS Laser," Appl. Phys. Lett. 33, 38 (1978).

12. S. Nita, H. Namizaki, S. Takamiya, and W. Susaki, "Single-Mode Junction-Up TJS Lasers with Estimated Lifetime of 10^6 Hours," IEEE J. Quantum Electronics QE-15, 1208 (1979).

CHAPTER III

INTEGRATION OF OPTICAL AND ELECTRONIC DEVICES

III.1 Introduction

In this chapter, methods will be described for the integration of both optical and electronic devices on a single chip. Consideration will be given to the monolithic compatibility of the various optical and electronic devices and the trade-offs which are encountered when they are monolithically fabricated. The first experiment in integration will be described in Section 2, in which a laser was fabricated together with a high frequency electronic oscillator to produce a modulated light source. In the third section, a brief review will be given of the theory of GaAs metal-semiconductor field effect transistor (MESFET) operation, and two general fabrication geometries will be described for the integration of a MESFET with a laser. In the fourth section, results will be given for the experimental verification of the feasibility of integrating a MESFET with a laser. In the final section, details will be given of an experimental device which consists of an optical detector, an electronic amplifier, and a laser. This device can be used to amplify an incoming optical signal, and can thus serve as a highly compact repeater for use in fiber optic communication systems.

III.2 Integration of a Laser with a Gunn Oscillator

The first demonstration of the integration of a laser with an electronic device was performed by integrating a CEL with a Gunn diode.[1] A Gunn diode is a bulk device which consists of nothing more than a sample of n-type GaAs with ohmic contacts applied to either side. Due

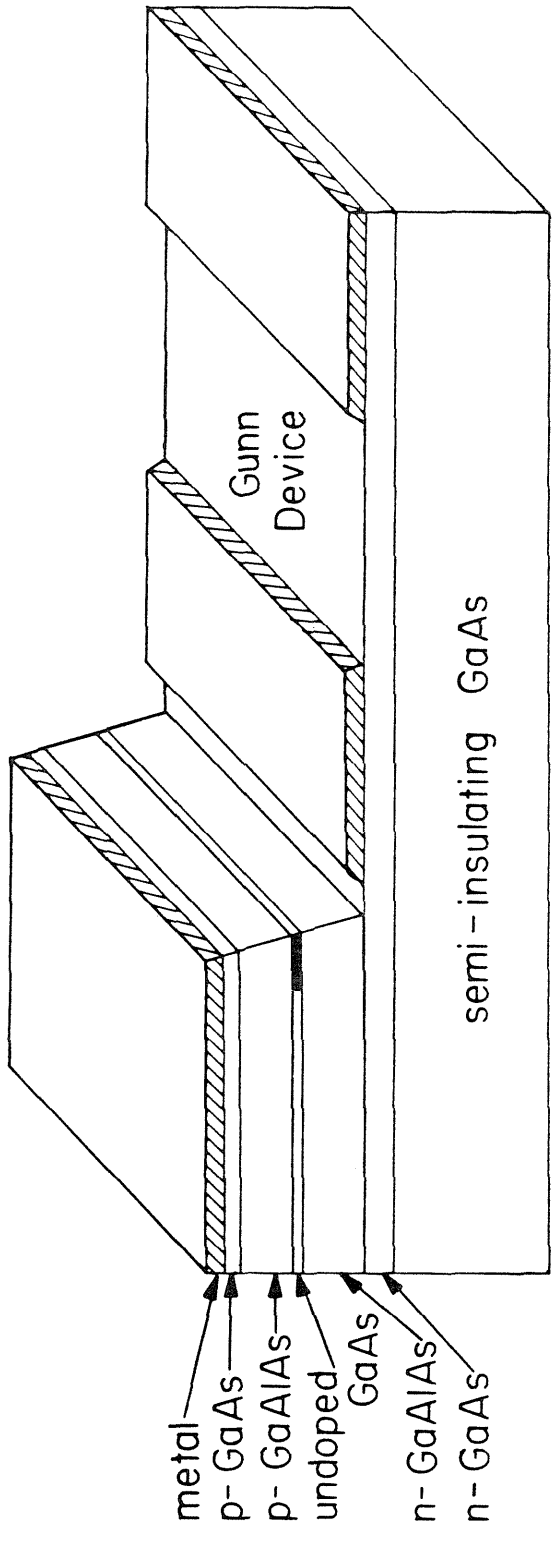

Fig. 3.1 A crowding effect laser which has been monolithically integrated with a Gunn oscillator

to intervalley scattering in the conduction band from a valley of small effective mass to a valley of large effective mass, GaAs exhibits a negative differential resistance over a range of electric fields.[2] For appropriate sample geometries, application of a static voltage to the contacts will lead to the formation of travelling but stable, high field domains. This behavior is known as the Gunn effect. Domains are nucleated at the cathode and travel toward the anode. Only one domain can exist in the sample at one time. Domain formation at the cathode and quenching at the anode proceed very rapidly, with the result that the oscillation frequency of the device depends primarily on the transit time of domains across the sample. The domain velocity is always somewhat lower than the peak electron velocity in the material, which in GaAs is $\sim 2 \times 10^7$ cm/sec. Transit time operation occurs for values of the product of the carrier concentration and device length,[2] $n_0 L > 10^{12} cm^{-2}$. The effect of field fringing outside the material sets a restriction on the minimum thickness of the active layer if stable domains are to develop. As a practical matter, the product of the doping concentration and the active layer thickness should be,[3] $n_0 d > 5 \times 10^{11} cm^{-2}$.

A schematic illustration of a combined crowding effect laser and Gunn device which was fabricated[1] is shown in Fig. 3.1. It is seen that the lower n-GaAs layer serves the dual function of providing the resistance necessary to achieve current crowding in the laser, and to form the Gunn diode.

The five epitaxial layers were all grown by liquid phase epitaxy (LPE) on a semi-insulating substrate. The doping of the lower n-GaAs layer

was chosen to be $\sim 10^{16} cm^{-3}$. The $Ga_{1-x}Al_xAs$ cladding layers have an aluminum mole fraction $x \sim 0.4$ and are doped with Sn and Ge to achieve n-type and p-type doping, respectively. The GaAs laser active layer is not intentionally doped, but is usually n-type. The layer thicknesses beginning with the layer closest to the substrate were 3, 2, 0.3, 2, and 1 μm.

Following growth of the epitaxial layers, Au-Zn was evaporated over the entire surface of the crystal. Laser mesas were then defined photolithographically and the surface on either side of the mesas was etched down to the n-GaAs layer. After etching, Au-Ge to form the n-type contact was deposited at an angle to the substrate normal. This procedure shadowed the mesa edges from being shorted by the metallization. The Gunn devices were defined by etching 140 μm-wide stripes in the Au-Ge metallization at a distance of 200 μm from the mesa edge.

The laser and the Gunn diode were operated in series as a single device. Because the lasers could not be operated cw, the devices were tested using 300 nsec, low duty cycle pulses. Results for one of the devices is shown in Fig. 3.2. The value of the threshold current for the laser was 170 mA. As can be seen in trace 2 of the figure, oscillations in the device occurred for currents above the threshold current of the laser. The result is that the light from the laser is less than 100% modulated, as can be seen in trace 1. The depth of modulation of the light is nonetheless far greater than that of the current, owing to the superlinear light vs. current relationship for a laser. Traces 3 and 4 correspond to traces 1 and 2, respectively, on an expanded time scale. The free-running oscillation frequency can be seen from the

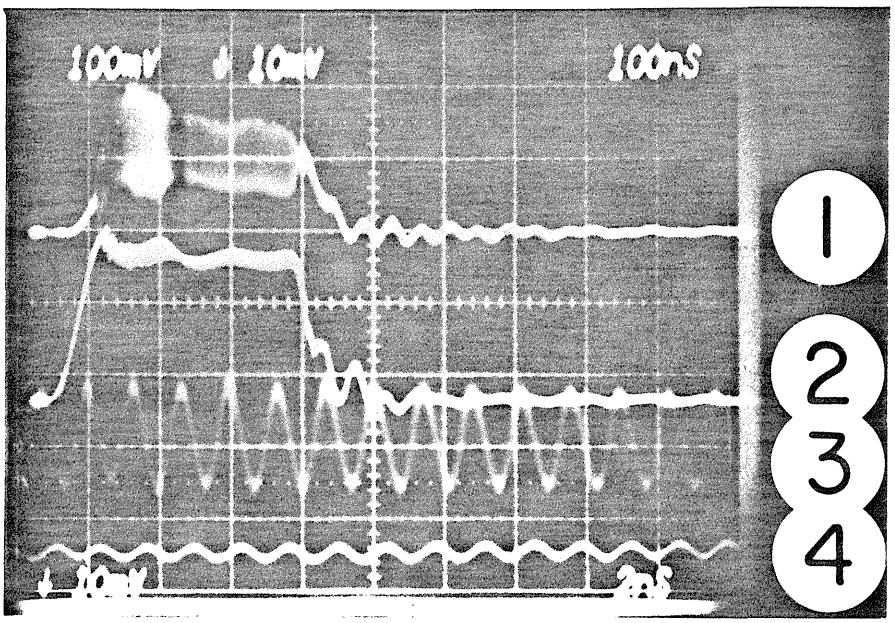

Fig. 3.2 Light output (trace 1, relative units) and current (trace 2, 100 mA/div) for an integrated laser-Gunn oscillator. Traces 3 and 4 are expanded views of traces 1 and 2, respectively.

figure to be $\sim$ 0.75 GHz, which corresponds to a domain velocity of $\sim 10^7$ cm/sec.

Gunn devices when operated as two terminal logic devices are nondirectional, and therefore can suffer from reflections and instabilities.[3] Three-terminal unidirectional Gunn devices have been demonstrated in which a Schottky gate near the cathode can be used to selectively nucleate a domain.[4] These devices can be used to perform various logic functions, but in general are far less flexible than the MESFET, which is the subject of the following section.

III.3 MESFET Theory and Fabrication

As was pointed out in Chapter I, the GaAs metal-semiconductor field effect transistor (MESFET) has enjoyed great success as a high speed electronic device. In this section a brief review of GaAs MESFET fundamentals will be presented, although for a more complete description the reader is referred to Ref. 5.

The principles of GaAs MESFET operation can be understood by referring to Fig. 3.3. Current in the device flows between the source and drain electrodes through a thin n-type electrically active layer. The layer is usually formed either by epitaxial growth or by ion implanting donors into the semi-insulating substrate. A buffer layer is sometimes inserted between the active layer and the substrate. A metal which forms a Schottky barrier on n-type GaAs, usually aluminum, is deposited in the channel which separates the source and the drain. This metal forms a gate which can be used to control the source to drain current. The gate controls the current by varying the thickness of the

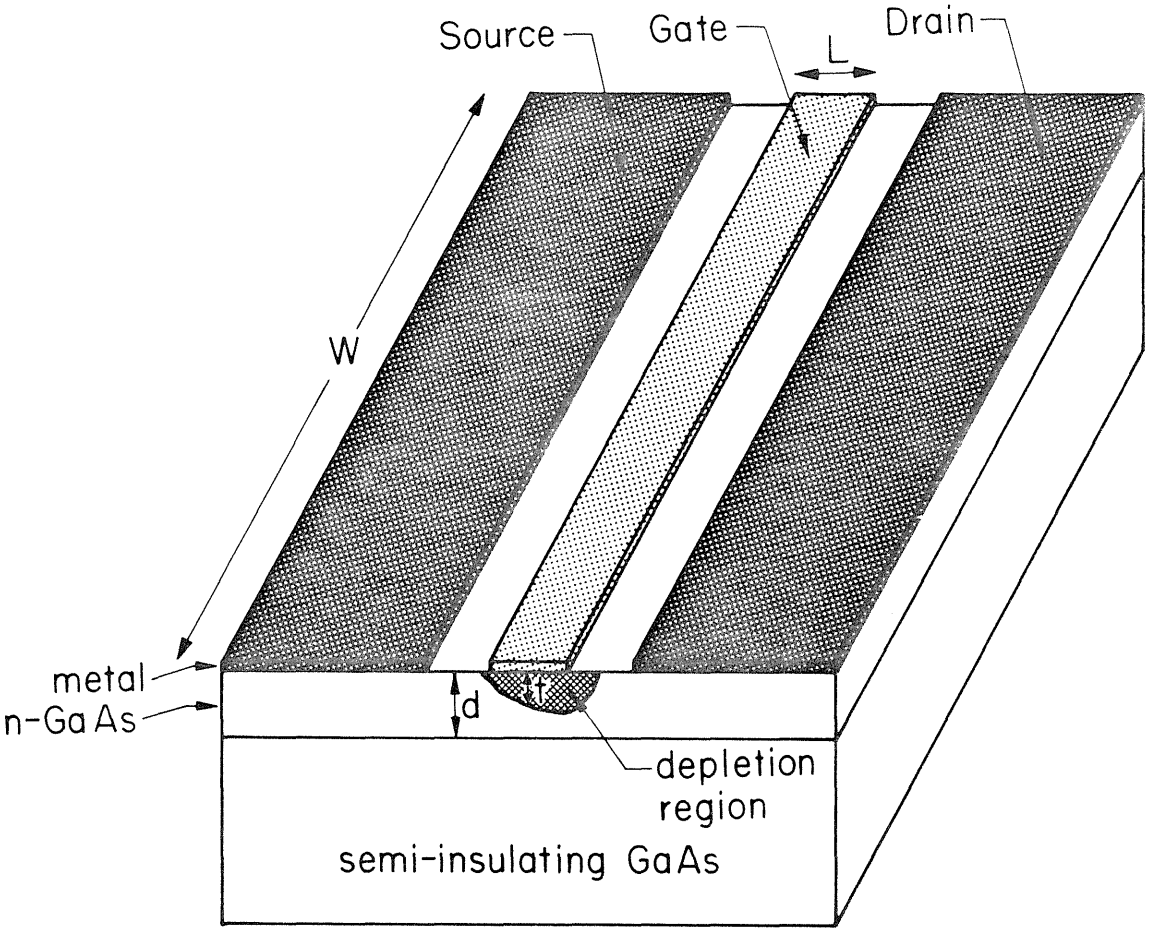

Fig. 3.3 The basic structure of a Schottky-gate metal-semiconductor field effect transistor (MESFET)

depletion region which removes carriers from the channel. Even with no external bias applied to the transistor, a depletion region forms under the gate due to the built-in voltage of the Schottky diode. By applying a negative bias to the gate with respect to the source, the depletion region can be enlarged to include even more of the channel thickness, or to even pinch off the channel entirely.

When a current flows between the source and drain, a lateral electric field is set up in the channel, and the gate to channel voltage is no longer constant under the gate. Since the drain is biased positively with respect to the source, the depletion region is largest at the drain side of the channel. Even if no bias has been applied to the gate, as the drain to source voltage is increased a point will be reached at which the depletion region constricts the channel to such a degree that the carriers crossing the channel must flow at their saturated velocity, and no further increase in the drain current with increasing drain voltage can be expected. The transistor is then said to be in saturation.

Using the notation of Fig. 3.3, we shall consider a device having a gate length L, gate width w, channel thickness d, depletion region thickness t(x), doping concentration N_D, and relative dielectric constant ε_r, which for GaAs[6] is ≃ 12.5. If we start with Poisson's equation for the potential in the depletion region,

$$\nabla^2 V = - \frac{qN_o}{\varepsilon_r \varepsilon_o} \tag{3.1}$$

and integrate across the depletion layer in the direction perpendicular

to the plane of the active layer, assuming the thickness of the depletion region to be slowly varying with x, we obtain

$$t(x) = \left(\frac{2\varepsilon_r \varepsilon_o V_j(x)}{qN_D}\right)^{1/2} \tag{3.2}$$

where V_j is the channel to gate voltage. If this voltage is sufficiently large, the channel will be pinched off, and from the previous expression, replacing t(x) by d, we define a pinch-off voltage,

$$V_p = \frac{qN_D}{2\varepsilon_r \varepsilon_o} d^2 \tag{3.3}$$

Values for the pinch-off voltage versus doping concentration for various channel thicknesses are shown in Fig. 3.4. It should be noted that the applied pinch-off voltage is lowered from V_p by the value of the built-in diode voltage V_b. For the case of an aluminum on GaAs Schottky barrier diode, V_b is given by [7]

$$V_b = 0.706 + 0.06 \log_{10}(10^{-16} N_D) \tag{3.4}$$

where V_b is in volts, and N_D is in units of cm^{-3}.

If we neglect the peak in the velocity versus field curve,[7] then the maximum amount of current which can flow in the channel with the gate absent is given by

$$I_s = qv_s N_D \, dw \tag{3.5}$$

where v_s is the saturation velocity of the carriers. With a gate present, current saturation occurs when the depletion region on the drain side has reached down far enough into the channel to cause the

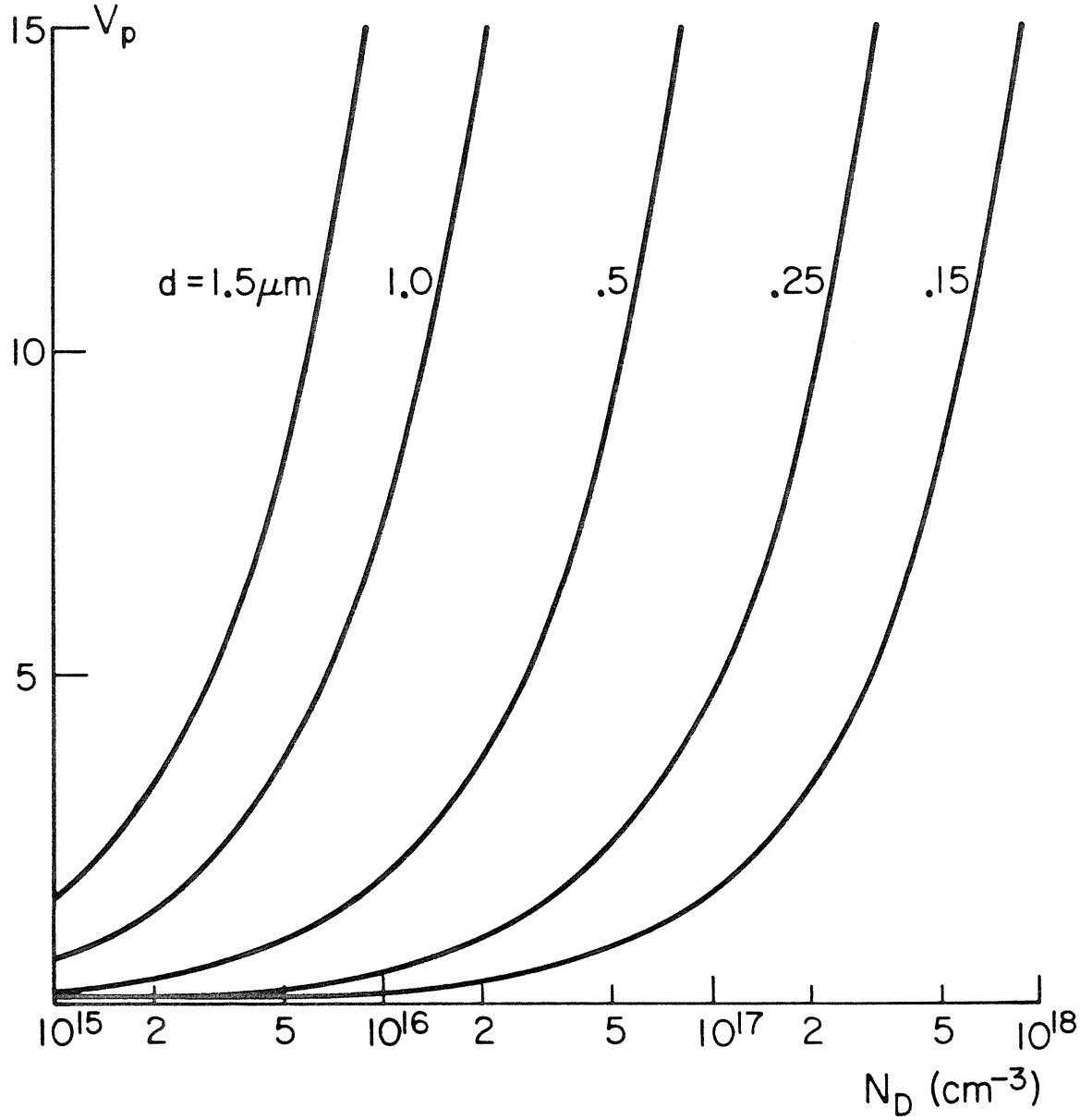

Fig. 3.4 The pinch-off voltage V_p (volts) for a GaAs layer of thickness d.

carriers underneath the depletion region to flow at their saturated velocity. This saturation current is given by

$$I_{sat} = qv_s N_D w(d - t_{sat}) \tag{3.6}$$

where t_{sat} is the thickness of the depletion region nearest the drain at which saturation sets in. If we consider the case when the source is grounded, then from equation (3.2) we obtain

$$t_{sat} = \left(\frac{2\varepsilon_r \varepsilon_o}{qN_D}\right)^{1/2} (V_{dsat} - V_g + V_b)^{1/2} \tag{3.7}$$

where V_{dsat} is the voltage on the drain at which saturation begins, and where V_g is the (negative) voltage on the gate. The ability of the gate to control the source to drain current I_d is described by the transconductance g_m, which from equations (3.3), (3.5), (3.6), and (3.7) can be found, in the saturation region of the I-V curves, to be given by

$$g_m \equiv \frac{\partial I_{dsat}}{\partial V_g} = \frac{I_s}{2V_p(1 - I_d/I_s)} \tag{3.8}$$

In order to integrate a MESFET with a laser on a single semi-insulating substrate, the structure of the epitaxial layers must be chosen so that they are compatible with the fabrication of both devices. In the devices which have been fabricated so far, two approaches have been taken. Both of these approaches make use of an LPE grown layer to form the MESFET channel, and are shown schematically in Fig. 3.5.

In the first case (Fig. 3.5a), the MESFET layer is grown directly on the substrate, and the entire laser double heterostructure is grown

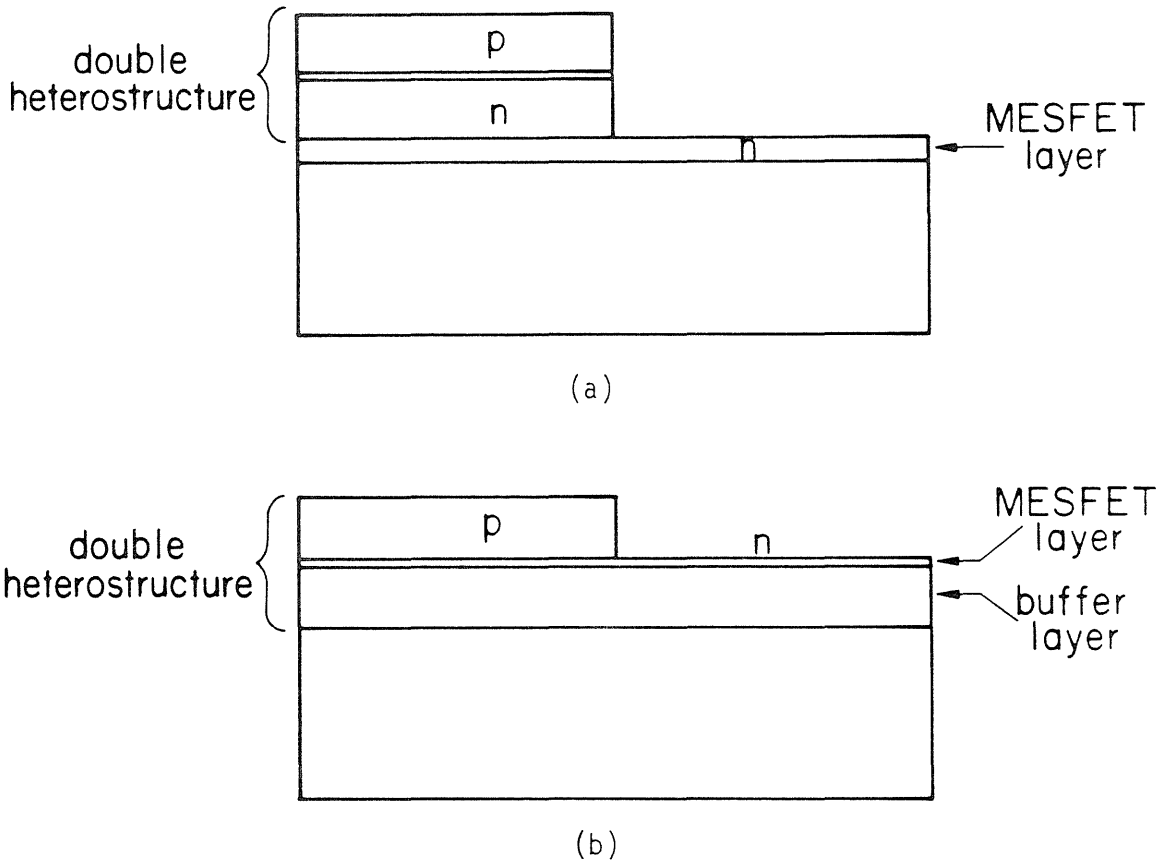

Fig. 3.5 Two general methods of integrating lasers and MESFETs on semi-insulating substrates. In (a) a separate layer is used to fabricate transistors, while in (b) the optically "active" layer of the laser also serves as the electrically "active" layer of the transistor.

on top of this layer. In the second case (Fig. 3.5b), a more complete crystallographic integration is achieved, with the MESFET and the laser sharing a common active layer. The laser and transistor can share a common layer without compromise because of the commonality of the two devices' layer parameter requirements. Both lasers and MESFETs are commonly made with active layer thicknesses in the range of 0.1-0.3 μm, and the amount of doping in a laser active layer is not critical. In addition, the lower GaAlAs cladding layer acts as a buffer layer for the MESFET by eliminating the influences of thermally induced conversion layers in the substrate.

The advantages of the second method are a lower number of layers, and the inclusion of a buffer layer which does not add to this count. The disadvantages of the second method are that the doping and thickness of the thin active layer must be very tightly controlled, and that the bottom cladding layer must be of sufficiently high resistivity so as not to introduce significant leakage currents.

In fabricating both of these structures, a laser mesa-defining etch must be performed down to the MESFET layer. To accurately halt the etch at the desired location, a two-step etching technique is employed. In the first step, an etchant which etches both GaAs and GaAlAs such as 1:8:8 H_2SO_4:H_2O_2:H_2O is used to etch down to the GaAlAs layer which lies directly above the MESFET layer. The remaining GaAlAs is etched away using hydrofluoric acid which etches GaAlAs, but does not attack GaAs. This can present a problem for the method of construction of Fig. 3.5b, since if any pinholes are present in the active layer, it may become undermined if allowed to stay in contact with the HF too long.

III.4 Integration of a T-Laser with a MESFET

As a first demonstration of the integration of a laser with a transistor, a low mesa T-laser and a MESFET were monolithically fabricated[8] using the design philosophy depicted in Fig. 3.5b. A schematic illustration of the combined device, along with a schematic diagram of the electrical circuit is shown in Fig. 3.6. The current which flows through the laser also flows through the transistor by virtue of their series connection in the common source configuration. The laser output is thus controllable by means of the voltage applied to the gate.

Fabrication of the device begins with a four-layer LPE growth. The thickness of the top p-GaAs contact layer is $\sim$ 0.5 μm, and the thickness of the $Ga_{1-x}Al_xAs$ ($x \sim 0.4$) cladding layers is $\sim$ 2 μm. The n-type GaAs active layer is doped nominally to a carrier concentration of $\sim 10^{17} cm^{-3}$ and has a thickness of 0.2-0.3 μm. The bottom GaAlAs cladding/buffer layer is either not intentionally doped or else very lightly doped with germanium to compensate for residual donors. Following growth, the crystal is coated with an evaporated film of Au-Zn. The "T" and the contact pad are defined by means of the two-step etch described in the last section. After etching, a layer of Au-Ge and Au is deposited to one side of the mesa. The Au overcoat is used to ensure a smooth and continuous film by preventing the Au-Ge contact from "balling up" when it is alloyed at 380°C.

The MESFET is fabricated using a self-aligned process. After coating the wafer with Shipley AZ1350J photoresist, a window is opened in the photoresist to define the gate region. The source and drain are

A Low Mesa T-Laser with an Integrated MESFET

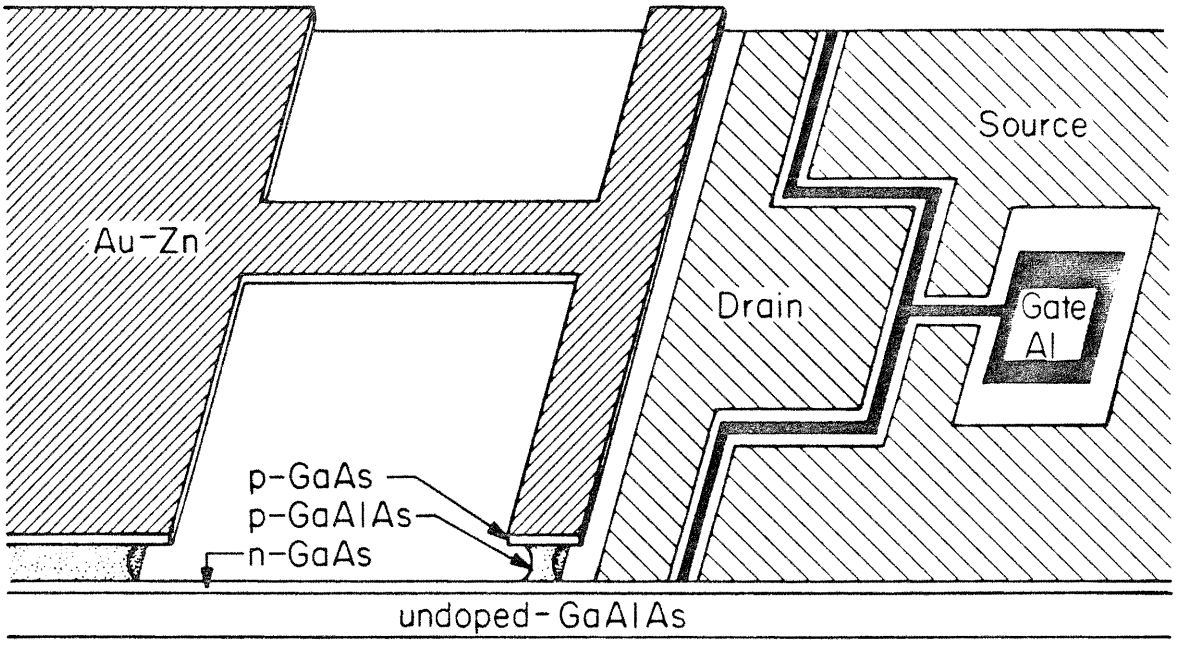

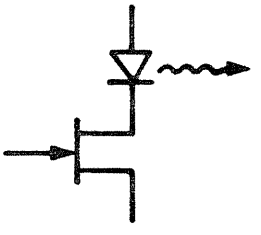

Schematic circuit

Fig. 3.6

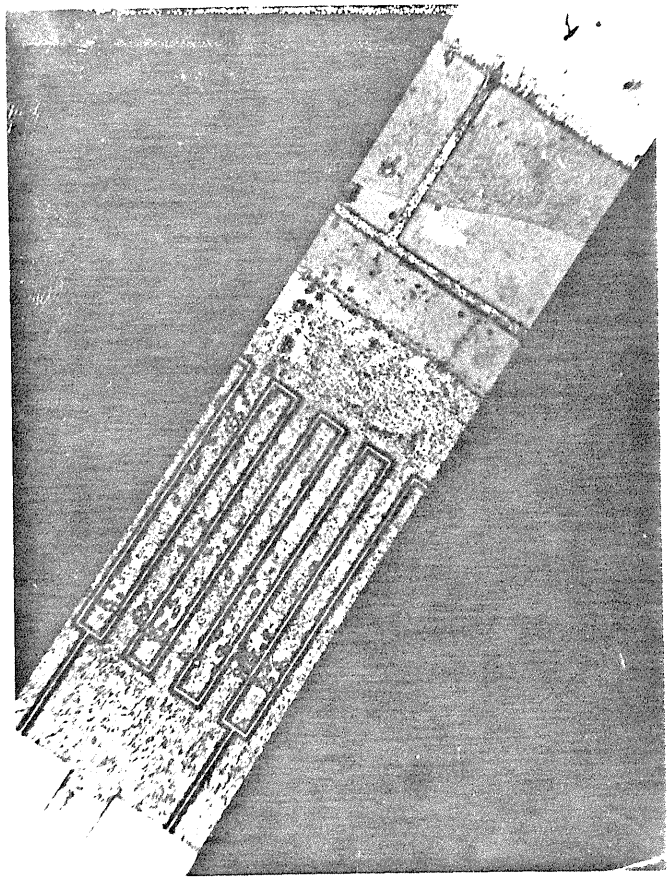

Fig. 3.7 A photograph of a T-laser integrated with a MESFET. The width of the chip is 390 μm.

formed by etching away the metallization in the gate region with a solution of KI + I_2. The etchant is allowed to slightly undercut the photoresist mask to effect a separation between the source, drain, and gate regions. Aluminum is next deposited on the sample with the photoresist still in place. The sample is then soaked in acetone, which dissolves the photoresist and lifts off the aluminum in the unwanted areas. A photograph of a typical device is shown in Fig. 3.7. Two gate pads are present because of the way in which the device was cleaved from a continuous row of devices.

Because the laser could not be run continuously without overheating, the device was operated on a pulsed basis. The effect of gate voltage on laser current for one device is shown in the upper oscilloscope trace in Fig. 3.8. The double curve is obtained by pulsing the anode voltage, with gate voltage as a parameter. The curve with the higher peak value of current corresponds to zero gate voltage, while the curve with lower current corresponds to a gate voltage of -5 V. The dimensions of the mesa stripe were 5 μm by 450 μm. A serpentine gate structure was employed whose dimensions were 10 μm by 5 mm. The relatively small observed change in current with gate voltage is explained by the fact that the saturation voltage of the transistor exceeded the Schottky gate breakdown voltage for this particular growth. This necessitated operating the transistor in the linear low transconductance region of the drain current-vs-voltage curve.

The height of the voltage pulse applied to the anode was chosen to limit the peak value of the current to just below the threshold current value of 110 mA, while a negative dc bias of -5 V was applied to the

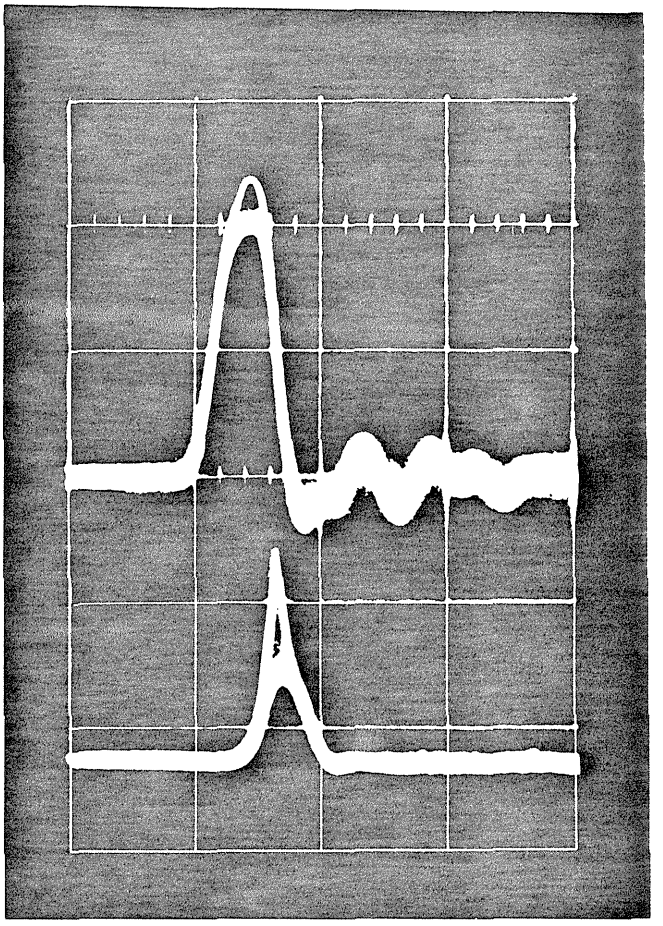

Fig. 3.8 Laser current (upper trace, 50 mA/div) and light output (lower trace, arbitrary units) for two values of gate voltage. In each trace, the larger peak corresponds to zero gate-to-source voltage, and the smaller peak corresponds to a gate-to-source voltage of -5 V. The horizontal scale is 1 μsec/div.

gate. The approximately 20 mA increase in peak current which resulted from applying zero gate voltage was sufficient to drive the laser above threshold, as is evidenced in the second trace of Fig. 3.8 by the superlinear dependence of light on current.

III.5 A Monolithically Integrated Optical Repeater

As a next step toward the development of more complicated monolithic optoelectronic circuits, an integrated optical repeater was conceived and built.[9] The repeater consists of an optical detector, an electronic amplifier, and a laser. The repeater can therefore be used to amplify and regenerate optical signals. This can be a very useful device in fiber optics communication systems in order to counteract the effect of optical loss and dispersion in fibers.

A schematic illustration of the repeater is shown in Fig. 3.9. The repeater consists of the three MESFETs Q_1, Q_2, Q_3 and a crowding effect laser. The transistors all reside on a common mesa, and the laser is situated at the edge of a second mesa which lies atop the first mesa. Transistor Q_1 forms a current source for biasing the optical detector Q_2, and Q_3 is the laser driver. A MESFET was chosen as the optical detector for ease of fabrication, and because it has been demonstrated to be a high sensitivity, high speed optical detector.[10,11,12] A crowding effect laser structure was used only for ease of fabrication.

The theory of operation of the repeater can be understood by referring to the schematic diagram of its electrical circuit which is shown in Fig. 3.10. The gate of Q_1 is biased such that with no optical signal present, a sufficiently large negative voltage appears at G_3 to cut off

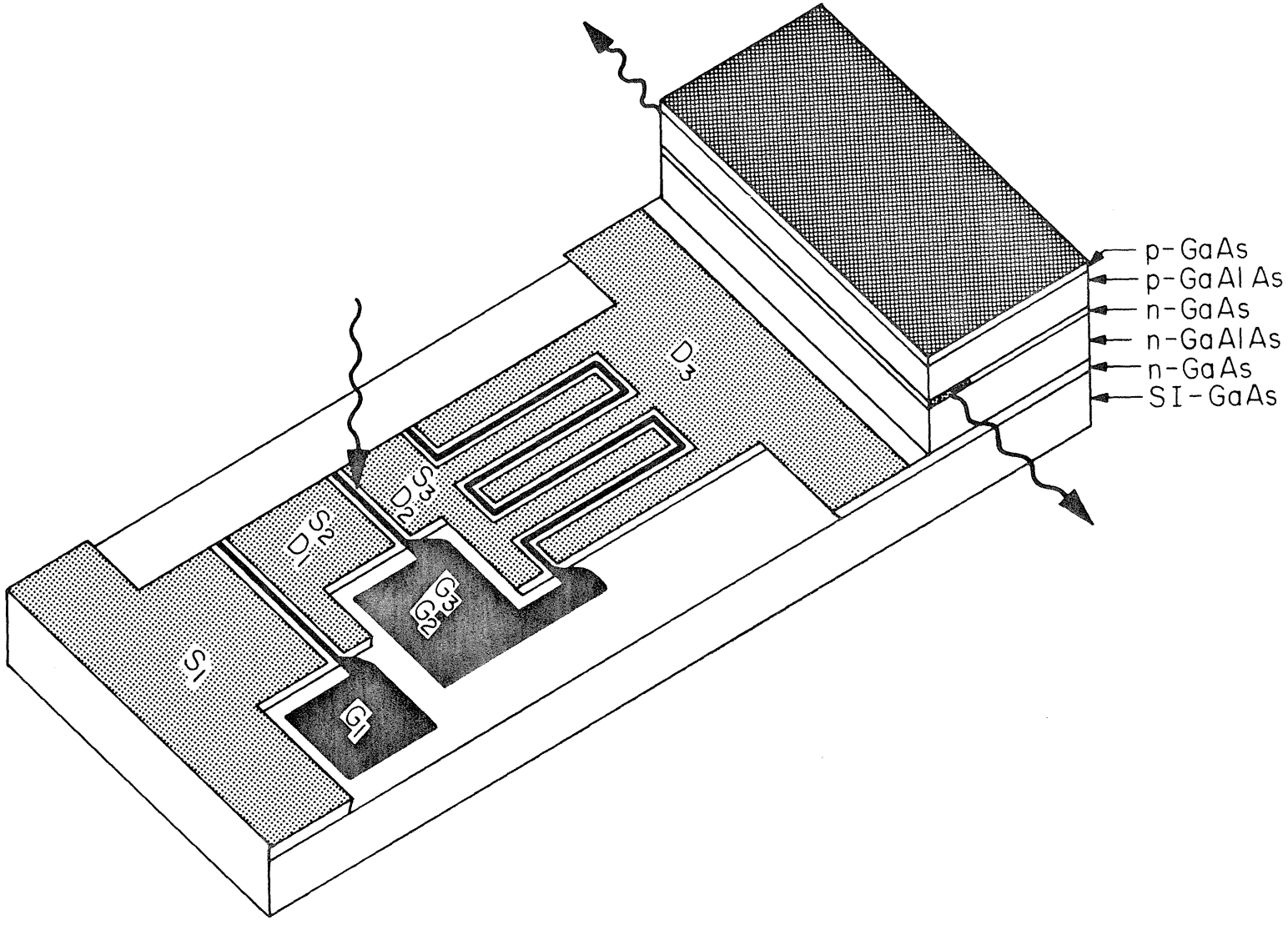

Fig. 3.9 A schematic illustration of the integrated optical repeater

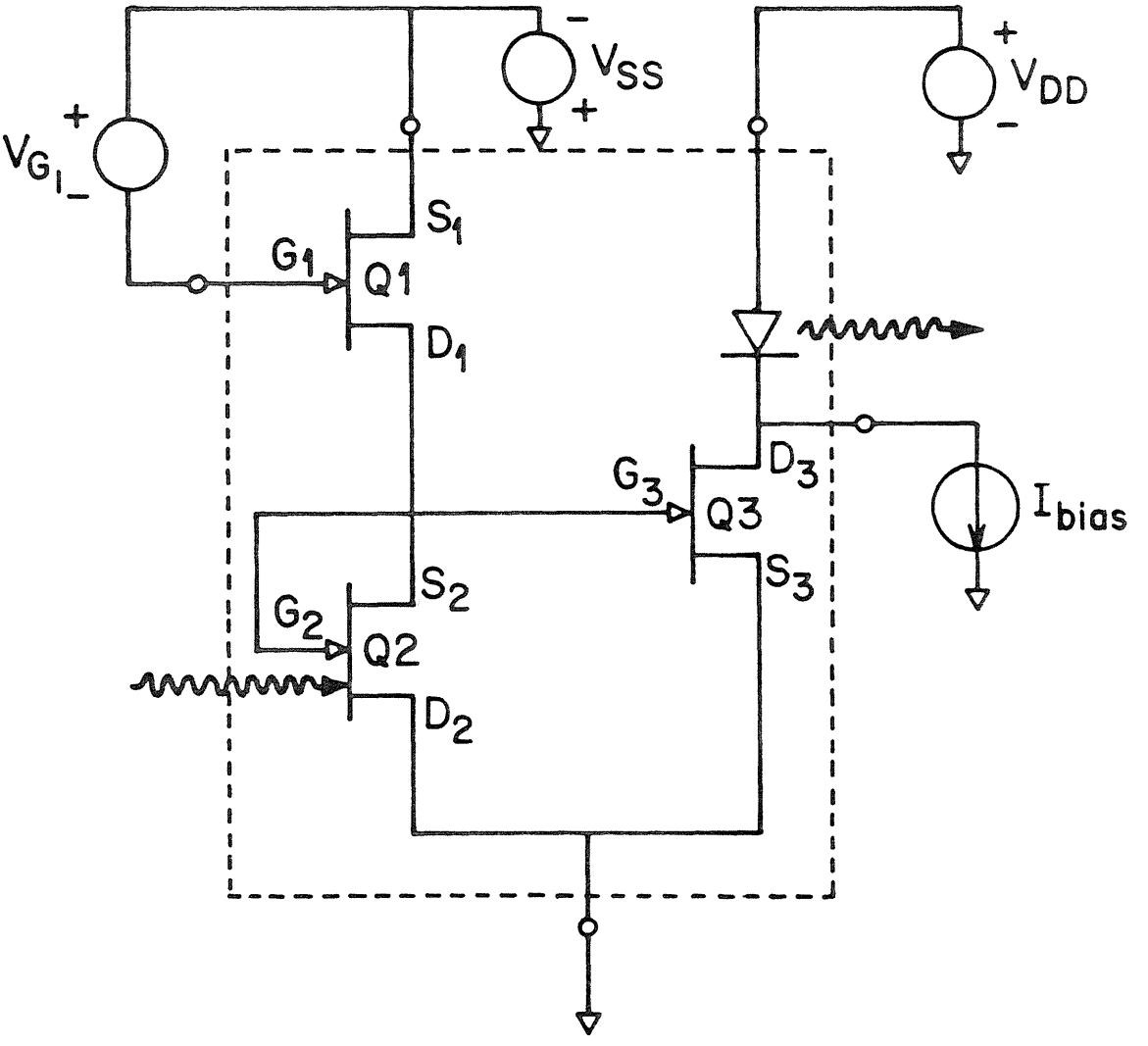

Fig. 3.10 A schematic circuit diagram of the repeater

Q_3. The only current which then passes through the laser is the external bias current which is adjusted to be close to the laser threshold value. When light is incident on the detector, photocarriers are generated in those areas of the channel not covered by the source, drain, or gate metallizations. We have found that illumination results in a change of the I-V curve of the detector as shown in Fig. 3.11. The I-V curve of the current source Q_1 serves as the load line for the detector. The application of an optical input to the detector therefore leads to a positive voltage change ΔV appearing at the gate of the driver, G_3. This causes Q_3 to conduct and to drive the laser current above threshold, thereby regenerating the optical input.

At the present time, the detailed mechanism of MESFET photoresponse is not fully understood. Three explanations have been proposed in the literature. In the explanation due to Gammel and Ballantyne,[11] the photoresponse is due to the increased conductivity of the channel beneath the depletion region. Thus the MESFET acts simply as a photoconductor, and was verified to exhibit photoconductive gain. Graffeuil et al.[13] argue that the generation of electron-hole pairs in the depletion region should appear as an effective gate voltage which is translated into a current change by the transconductance of the transistor. According to Sugeta and Mizushima,[12] the change in drain current is due to two components. The first component is due to the current collected by the Schottky diode in the gate drain region, and the second component is due to an actual change in gate voltage, which results when the gate-current flows in the resistance between gate and ground. The decision on which theory is correct must await further investigation.

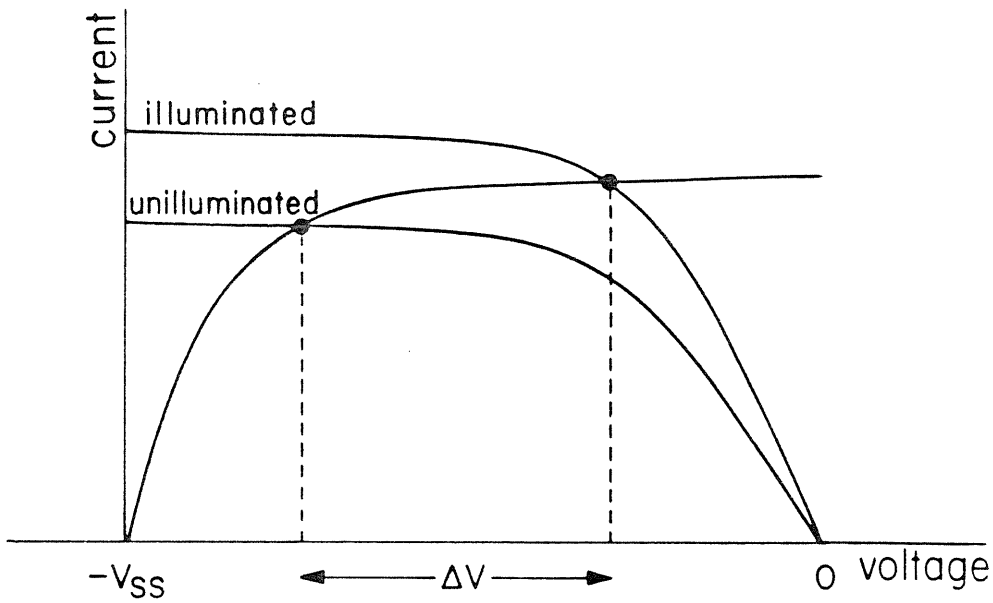

Fig. 3.11 The I-V curves of transistors Q_1 and Q_2. The point of intersection of the curves determines the voltage that appears at the gate of Q_3.

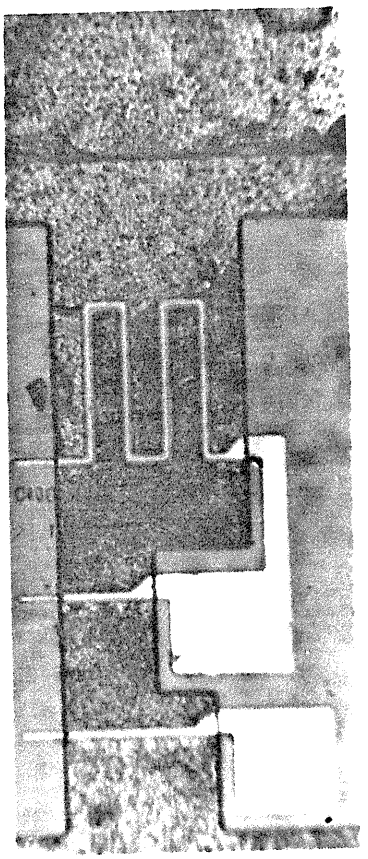

Fig. 3.12 A photograph of an integrated optical repeater

Fabrication of the repeater begins with a five-layer LPE growth on a (001) substrate. After evaporating Cr-Au to form the p-type contact, a mesa is etched along the $[1\bar{1}0]$ direction to form the laser. The laser mesa is formed by first etching through the laser active layer and midway into the n-GaAlAs layer, and finally by etching the remaining GaAlAs using HF as a selective etchant. The exposed n-GaAs layer can then be partially etched to obtain the desired transistor characteristics. Metallization for the n-type contacts is applied by shadow evaporating Au-Ge and Au from the direction of the laser mesa. The transistor mesa is defined by etching the surrounding area with 1:8:8 (H_2SO_4:H_2O_2:H_2O) down to the semi-insulating substrate. Use of this etchant results in inclined mesa edges whose slope depends on the orientation of the mesa on the substrate. The device orientation is chosen such that those mesa edges which are to be covered by gate metallization are properly sloped to ensure complete coverage by the deposited metal. The Schottky gates are formed using the self-aligned process to deposit the aluminum gates between the source and drain metallizations, which was described in the previous section. After alloying the Au-Ge contacts, the substrate is thinned to a thickness of $\sim$ 100 μm, and the wafer is cleaved into individual devices whose dimensions are nominally 425 x 1500 μm. A photograph of a typical device is shown in Fig. 3.12.

Results will be given for a device whose layer parameters are given in Table 3.1. The layers are numbered starting at the substrate. The bottom n-GaAs layer had a final thickness after etching of $\sim$0.6 μm.

Table 3.1 Layer Parameters of the Repeater

Layer	Composition	Doping	Thickness
1	n-GaAs	$2 \times 10^{16} cm^{-3}$	1.4 μm
2	n-$Ga_{0.5}Al_{0.5}As$	10^{17}	2.1
3	n-GaAs	10^{17}	0.3
4	p-$Ga_{0.5}Al_{0.5}As$	10^{18}	2.1
5	p-GaAs	10^{19}	1.0

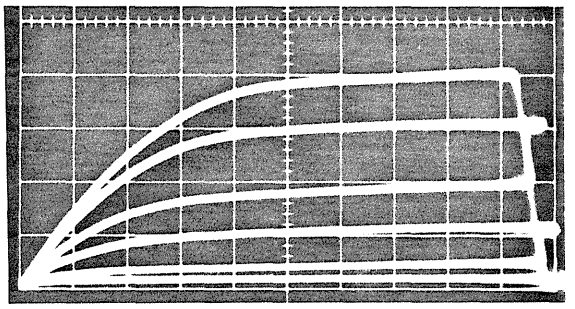

(a)

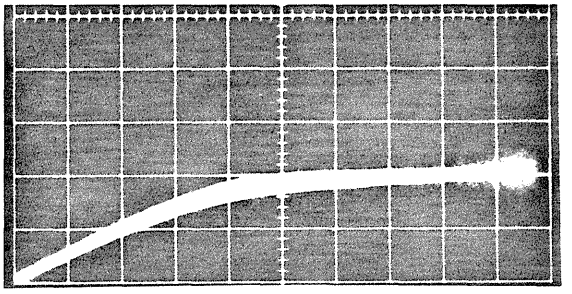

(b)

Fig. 3.13 I-V curves of (a) transistor Q_1 for several values of gate voltage, and (b) transistor Q_2 with the gate shorted to the source. The horizontal scale is 1 V/div and the vertical scale is 2 mA/div. In (a) the gate voltage is incremented at 1 V/step.

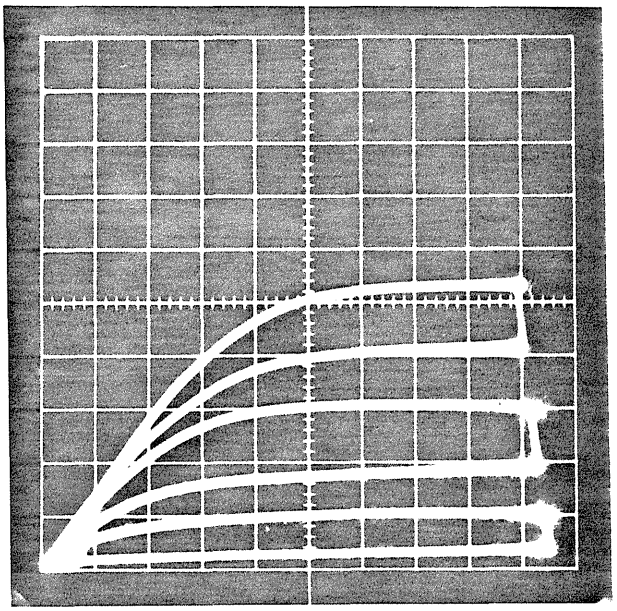

Fig. 3.14 I-V curve of transistor Q_3. The horizontal scale is 1 V/div and the vertical scale is 10 mA/div. The gate voltage is incremented at 1 V/step.

The gate length for the transistors was 5 μm, and the pinch-off voltage was 5 V. The characteristic curves of the transistors are shown in Figs. 3.13 and 3.14. The transconductance of Q_3 was measured to be $\sim$ 12 millimho. The laser had a length of 480 μm, a room temperature pulsed threshold current of 400 mA, and a differential quantum efficiency of 5 percent per facet.

Because the laser did not operate cw, the repeater had to be operated on a pulsed basis. This was accomplished by using a pulse generator to supply V_{DD}, and by using an n-channel silicon FET as a current source to supply the laser bias current. The gate voltage of the VFET was adjusted to bias the laser just above threshold for the duration of the power supply pulse. The response of the laser in the absence of an optical input pulse can be seen in Fig. 3.15a.

Light having a wavelength of 850 nm was introduced to the detector from an external GaAlAs laser by means of an optical fiber. The excitation of the external laser was timed to synchronize with the application of the power supply pulse to the repeater. With 140 μW of optical power incident on the active area of the detector Q_2, an increase in the light output from one of the laser facets of about 700 μW was observed, as can be seen in Fig. 3.15b. This corresponds to an overall optical gain of about 10 dB when light from both laser facets is considered.

Although thermal effects prevented operating the repeater in a cw mode, it is felt that by replacing the laser with one possessing a lower value of threshold current, cw repeater operation should be

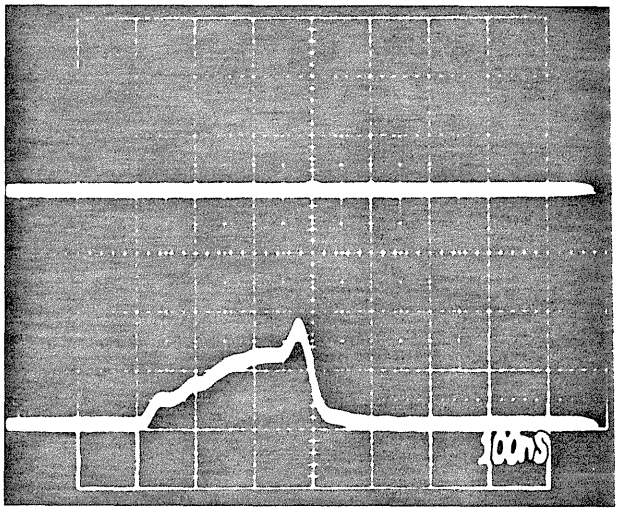

(a)

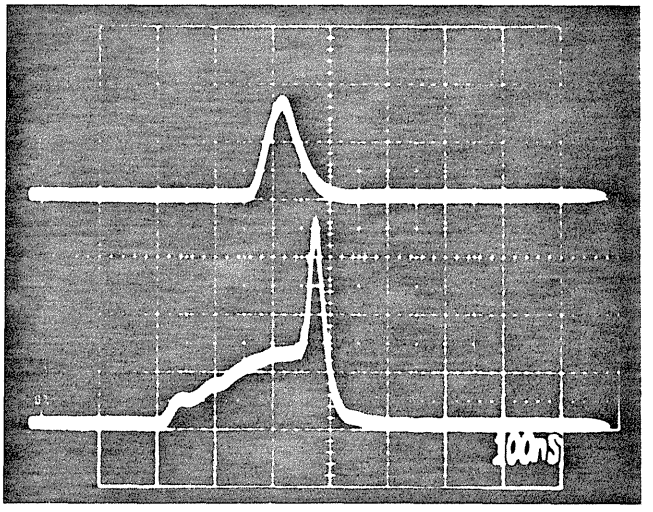

(b)

Fig. 3.15 Response of the repeater (a) with no optical input, and (b) with optical input. The upper traces correspond to the current through the external laser in relative units. The lower traces correspond to light (350 μW/div) from one of the repeater's laser facets.

attainable. TJS lasers have been fabricated with the heat sink attached to the semi-insulating substrate, and have been successfully operated at temperatures up to 110 C.[14] This seems to indicate that power dissipated in the electronic portion of an integrated optoelectronic circuit will not seriously degrade the laser performance.

REFERENCES FOR CHAPTER III

1. C. P. Lee, S. Margalit, I. Ury, and A. Yariv, "Integration of an Injection Laser with a Gunn Oscillator on a Semi-Insulating GaAs Substrate," Appl. Phys. Lett. 32, 806 (1978).
2. S. M. Sze, Physics of Semiconductor Devices, Wiley-Interscience, New York (1969).
3. H. L. Hartnagel, Gunn-Effect Logic Devices, American Elsevier Publishing Company, Inc., New York (1973).
4. T. Sugeta and H. Yanai, "Schottky-Gate Bulk-Effect Digital Devices," Proc. IEEE 59, 1629 (1971).
5. C. A. Liechti, "Microwave Field-Effect Transistors--1976," IEEE Trans. Microwave Theory and Techniques MTT-24, 279 (1976).
6. H. Fukui, "Determination of the Basic Device Parameters of a GaAs MESFET," Bell System Tech. J. 58, 771 (1979).
7. H. Fukui, "Channel Current Limitations in GaAs MESFETs," to be published.
8. I. Ury, S. Margalit, M. Yust, and A. Yariv, "Monolithic Integration of an Injection Laser and a Metal Semiconductor Field Effect Transistor," Appl. Phys. Lett. 34, 430 (1979).
9. M. Yust, N. Bar-Chaim, S. H. Izadpanah, S. Margalit, I. Ury, D. Wilt, and A. Yariv, "A Monolithically Integrated Optical Repeater," Appl. Phys. Lett. 35, 795 (1979).
10. C. Baach, G. Elze, and G. Wolf, "GaAs MESFET: A High-Speed Optical Detector," Electron. Lett. 13, 193 (1977).

11. J. C. Gammel and J. M. Ballantyne, "The OPFET: A New High Speed Optical Detector," Proc. IEDM, 120 (1978).

12. T. Sugeta and Y. Mizushima, "High Speed Photoresponse Mechanism of a GaAs-MESFET," Jap. J. Appl. Phys. 19, L27 (1980).

13. J. Graffeuil, P. Rossel, and H. Martinot, Electron. Lett. 15, 440 (1979).

14. H. Kumabe, T. Tanaka, H. Namizaki, M. Ishii, and W. Susaki, "High Temperature Single Mode CW Operation with a Junction-Up TJS Laser," Appl. Phys. Lett. 33, 38 (1978).

CHAPTER IV

WHISPERING GALLERY LASERS

IV.1 Introduction

In each of the more complex optoelectronic circuits described in the preceding chapter, the integrated laser relied in the conventional way on two opposite cleaved facets to provide the optical feedback necessary to support lasing. When one considers fabricating significantly more complex integrated optoelectronic circuits, one is faced by a restriction imposed on one of the chip dimensions by the length of the laser cavity. Injection lasers are typically not made much longer than 300μm because any increase in length results only in a larger value of threshold current and a reduced differential quantum efficiency.[1] To eliminate this rather serious restriction on the chip size, one can consider replacing one of the cleaved mirrors with either an etched mirror,[2] distributed feedback, or a distributed Bragg reflector formed by an etched grating.[3] All of these methods however, introduce substantial optical losses. An alternative solution, which is the subject of this chapter, is to curve the optical path in the laser cavity so that a resonator may be formed at either a single cleaved facet or at a cleaved corner.

Light can be made to follow the curve of a dielectric interface by the mechanism of total internal reflection in much the same way that sound waves can be made to propagate along the curved walls of a whispering gallery. Perhaps the most famous whispering gallery of this type

occurs along an elevated curved walkway at the base of the dome inside St. Paul's Cathedral in London. The mechanism by which two people at any two points along the walkway can hear each other whisper was first correctly explained by Lord Rayleigh.[4] Dielectric discs have been proposed for use as high-Q optical resonators,[5] and injection lasers based on this principle have been fabricated on n^+-GaAs substrates.[6]

In the next section, details will be given of the fabrication procedure for obtaining whispering gallery lasers on semi-insulating GaAs substrates, along with performance results for these devices. In Section 3, a detailed description will be given of the modes which propagate in whispering gallery lasers. The fourth section will present a general scattering theory for a perturbed dielectric resonator. In the final section these results will be applied to the case of a whispering gallery laser having a rough surface.

IV.2 Fabrication and Operating Characteristics

The structure which was chosen for the fabrication of the whispering gallery lasers is identical to the structure of the crowding effect laser of Section II.2. In this case though, the polarity of the device was chosen such that the n-type layers are on top. This was done to reduce the sheet resistance of the upper layers, and because the contact resistance to n-type layers is usually smaller. As was shown in Chapter II, reduction of these two factors decreases current spreading and leads to lower values of threshold current. A schematic illustration of the devices is shown in Fig. 4.1, and a description of the layers is given in Table 4.1.

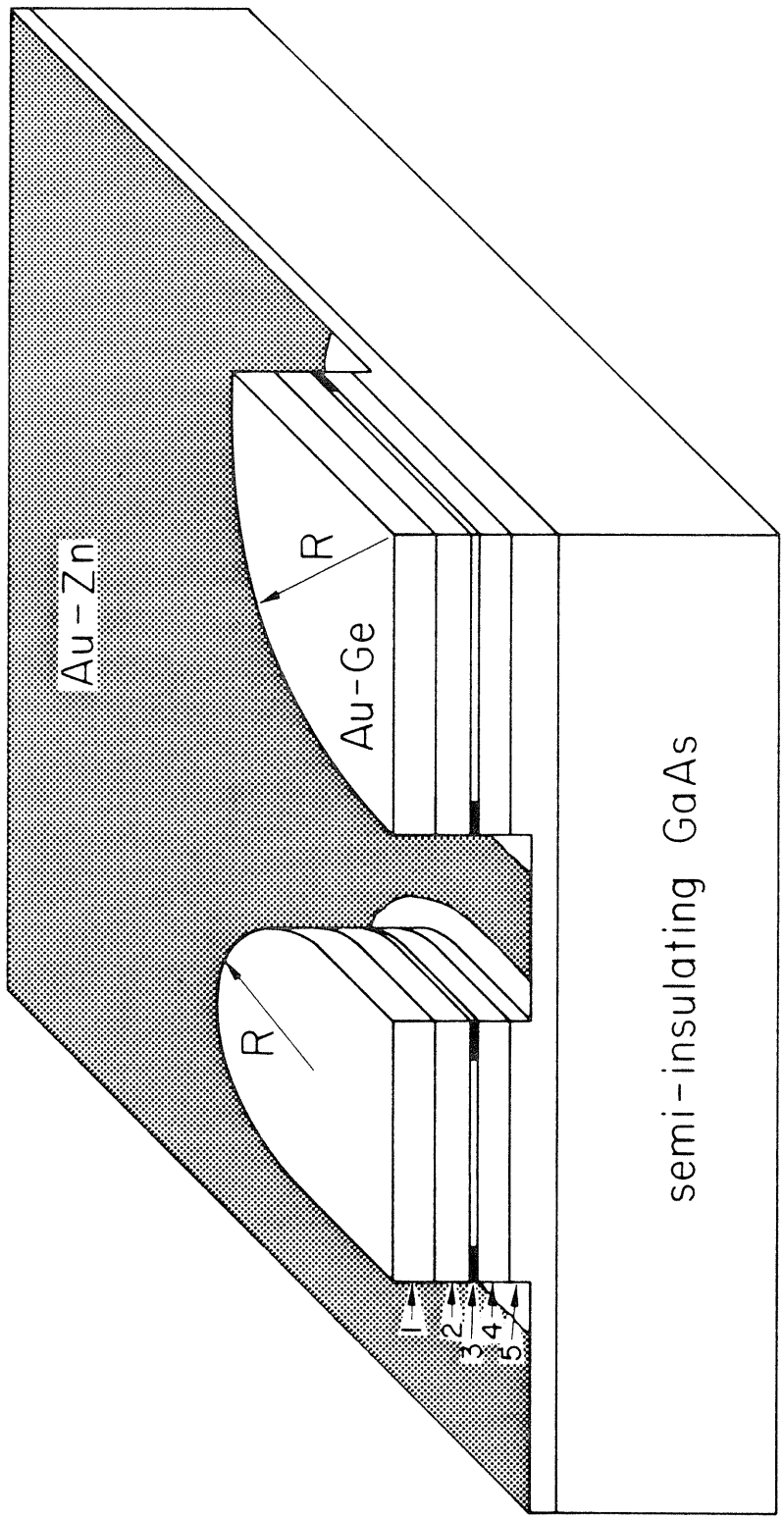

Fig. 4.1 Schematic diagram of a quarter ring and a half ring whispering gallery laser

When current is passed through the laser, the bulk of the injected current, and hence the optical gain, is restricted to a region lying within just a few microns of the mesa edge as a result of the crowding effect. As will be seen in Section IV.3, the widths of the fundamental optical modes of the laser are also on the order of several microns for values of the parameters typical for these devices. Thus both the optical modes and the gain region are restricted to the immediate vicinity of the mesa edge, a condition needed to assume a maximum gain for a given injection current.

Table 4.1 Parameters of the Grown Layers

Layer	Composition	Doping	Thickness
1	n-GaAs	5×10^{18} cm^{-3}	2.5
2	n-$Ga_{0.6}Al_{0.4}As$	10^{17}	2.0
3	undoped GaAs	-	0.25
4	p-$Ga_{0.6}Al_{0.4}As$	10^{17}	2.0
5	p-GaAs	10^{17}	2.5

The devices were fabricated beginning with a liquid phase epitaxy growth of the layers, followed by a deposition of Au-Ge and Au to a thickness of 1 μm. Resist patterns were photolithographically defined, and metal was etched in the exposed areas. The Au patterns were used as an etching mask for mesa definition. The mesas were etched using a solution of 3 methanol:1 phosphoric acid:1 H_2O_2, which is known to etch GaAs in a very smooth fashion.[2] The metal overhang which resulted from

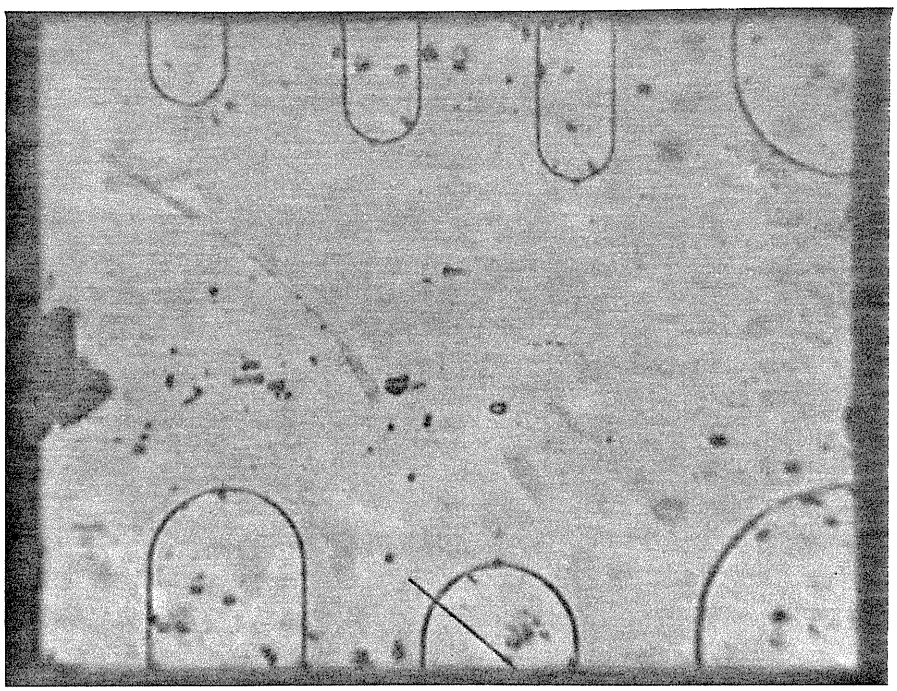

Fig. 4.2 A photograph of a chip on which several whispering gallery lasers have been fabricated

lateral etching was used as a shadow mask for the evaporation of the Au-Zn p-type contact. Both half-ring and quarter-ring lasers were fabricated with radii ranging from 45 to 195 μm. The curved sections were terminated by straight sections to facilitate cleaving. Straight control lasers were also fabricated from the same wafer. A photograph of a chip with devices whose radii are 45, 95, 145, and 195 μm is shown in Fig. 4.2.

The straight lasers displayed room temperature pulsed threshold currents which were as low as 36 mA for a 100 μm long device. The best differential quantum efficiency obtained for the straight lasers was 32%. The best performance for a curved laser was observed in a 145 μm-radius quarter-ring laser, which had a threshold current of 180 mA, and a differential quantum efficiency of 10%. The spectra of a half-ring and a quarter-ring laser are shown in Fig. 4.3. The spacing between the modes is proportional to the reciprocal of the sum of the arc length of the curve and the length of the straight sections. The near field pattern for a half-ring laser is shown in Fig. 4.4, which suggests that lasing is occurring among several radial modes.

Since the threshold current values for the curved lasers were higher than those for the straight control lasers, it would seem that there is some optical loss mechanism associated with the curved sections. The value of the loss constant α_c along the curve can be deduced from the measured value of the threshold current by means of the oscillation condition

$$g(L_s + L_c) = \ell n(1/R) + \alpha^o(L_s + L_c) + \alpha_c L_c \qquad (4.1)$$

where g is the optical gain, L_s and L_c are the lengths of the straight and

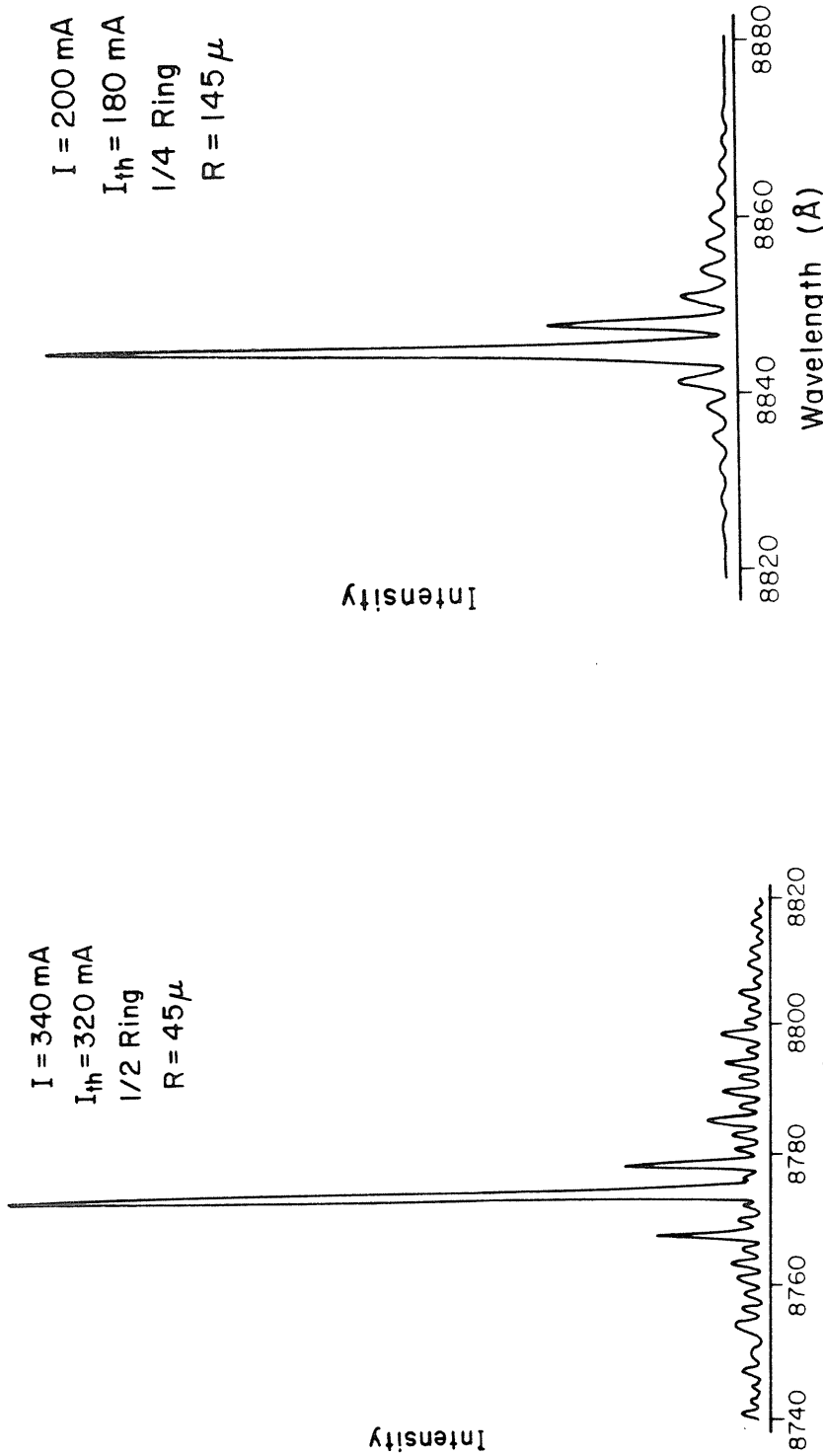

Fig. 4.3 Emission spectrum of (a) a half ring laser, and (b) a quarter ring laser

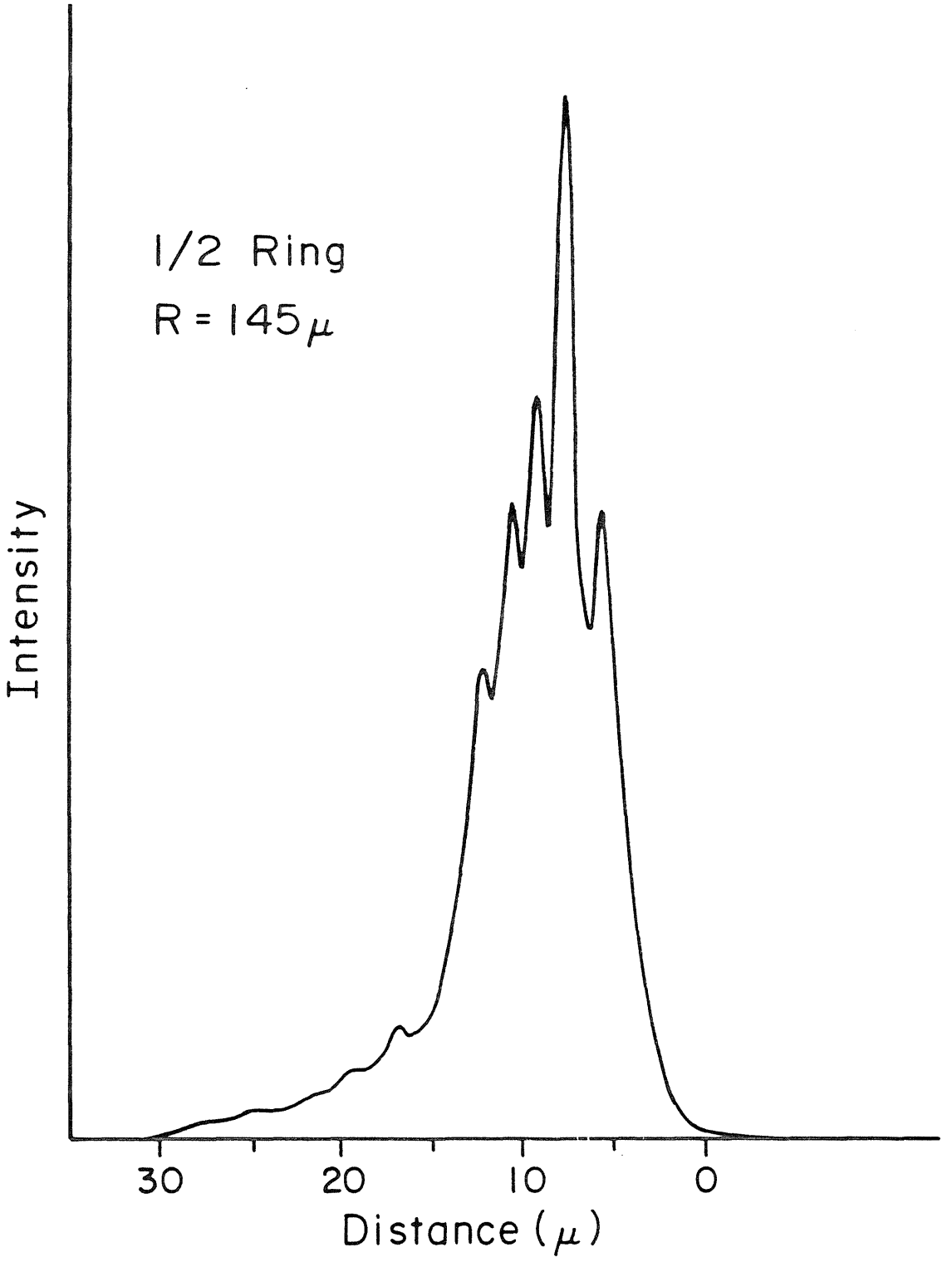

Fig. 4.4 Near field pattern of a half ring laser. The origin is at the mesa edge.

curved sections respectively, R is the facet reflectivity, and α^o represents all other optical losses. If we assume that the width of the gain region does not vary much with injection current, we can take the gain to vary linearly with pumping current density[7] in A/cm, which we express as

$$g = \frac{1}{A} \frac{I}{L_s + L_c} - J_o \tag{4.2}$$

where A and J_o are constants to be determined. Combining equations (4.1) and (4.2) we obtain for the threshold current of the straight lasers,

$$I_s^{th} = (A\alpha^o + J_o)L_s + A\, \ell n(1/R) \tag{4.3}$$

By analyzing the data for a number of straight lasers, we obtain the values A = 18 mA and J_o = 1.0 A/cm, assuming a loss constant $\alpha^o = 50\ cm^{-1}$. The values of α_c can be determined by combining equations (4.1) and (4.2) to yield

$$\alpha_c = \frac{I_c^{th}}{AL_c} - \frac{\ell n(1/R)}{L_c} - (\alpha^o + J_o)(1 + \frac{L_s}{L_c}) \tag{4.4}$$

where I_c^{th} is the threshold current value for a curved laser. Values of α_c determined by equation (4.4) are plotted in Fig. 4.5. The straight line in Fig. 4.5 represents a least squares fit to the data for a straight line passing through the origin.

The inevitable radiation loss from a perfectly smooth curved dielectric boundary is not large enough to explain the observed optical losses, as will be shown in the next section. The origin of the optical losses seems to be from scattering at the rough surface of the etched mesa. This

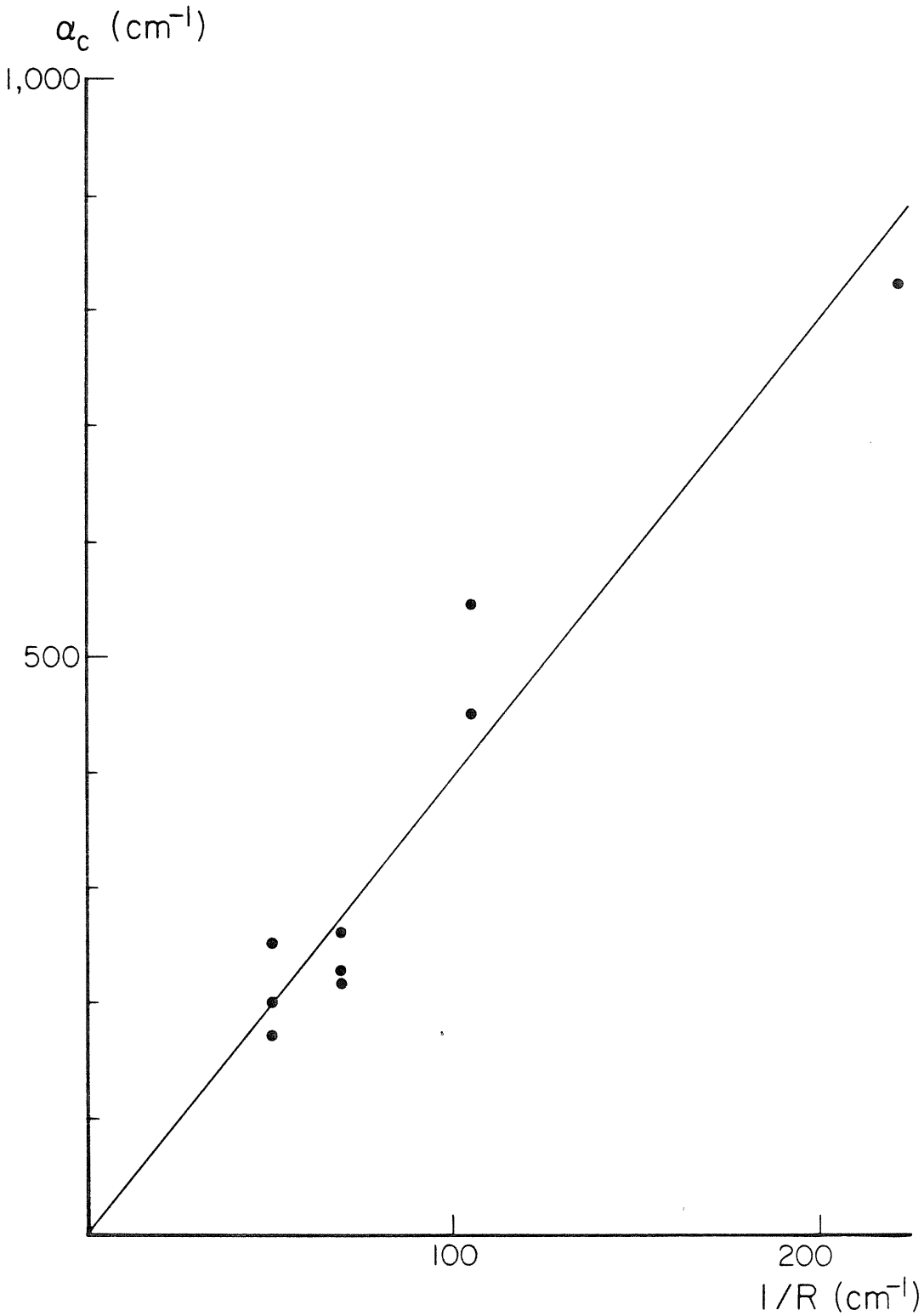

Fig. 4.5 Loss constant versus reciprocal radius for guiding along the curved interface

will be discussed in Sections 4.4 and 4.5. This indicates that an improvement in the performance of these devices could be obtained by improving the smoothness of the mesa edge, or by reducing the index step at the mesa edge, which would reduce its "optical" roughness.

IV.3 Optical Modes

In this section, an analysis will be made of the quasi-bound optical modes that propagate in a whispering gallery laser. Special emphasis will be placed on those modes which are most closely confined to the vicinity of the dielectric interface. The analysis will be performed on a full ring laser, although the results apply equally well to half-ring and quarter-ring lasers.

The GaAs active layer of a full-ring laser is in the shape of a disc of radius R, whose refractive index will be denoted by n_2. The upper and lower GaAlAs cladding layers can be modelled by semi-infinite cylinders of index n_1 and n_3, respectively. The composite infinite cylinder is surrounded by air with refractive index $n_0 \simeq 1$. Definitions of the polar coordinates to be used are given in Fig. 4.6.

If we assume an $e^{i\omega t}$ time dependence for all field components, Maxwell's curl equations can be written in the form

$$\begin{aligned} \nabla \times \vec{H} &= i\varepsilon\omega\vec{E} \\ \nabla \times \vec{E} &= -i\mu\omega\vec{H} \end{aligned} \tag{4.5}$$

Combining these two equations, we can write a wave equation in each of the regions of uniform refractive index,

$$(\nabla^2 + k_m^2)\psi = 0 \tag{4.6}$$

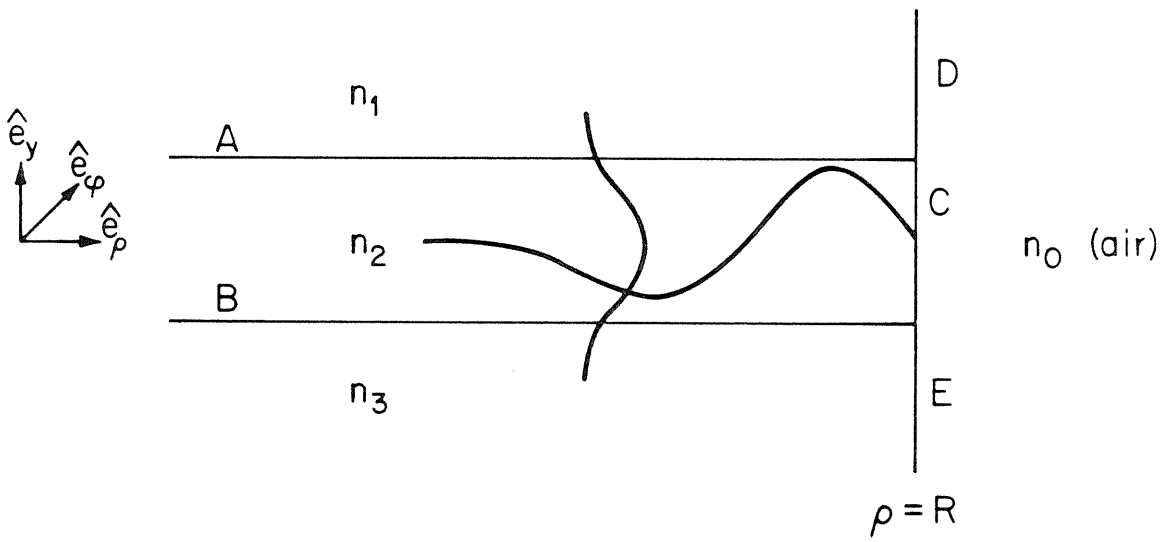

Fig. 4.6 A cross-section of the model used to describe the optical modes of the whispering gallery laser. The mode which is shown is zeroth order in the y-direction, and first order in the radial direction.

where ψ represents a component of either $\vec{E}$ or $\vec{H}$, and where $k_m \equiv n_m\omega/c$. Since the wave equation (4.6) is separable in polar coordinates, we can express ψ as a product of three functions,

$$\psi = R(\rho)\ Y(y)\ \Phi(\phi) \tag{4.7}$$

If we insert equation (4.7) into (4.6), we obtain the following equations:

$$\begin{aligned} \rho^2 \frac{d^2R}{d\rho^2} + \rho \frac{dR}{d\rho} + [(k_m^2 - k_{ym}^2)\rho^2 - \nu^2]R &= 0 \\ \frac{d^2Y}{dy^2} &= -k_{ym}^2 Y \\ \frac{d^2\Phi}{d\phi^2} &= -\nu^2\Phi \end{aligned} \tag{4.8}$$

where ν^2 and k_{ym}^2 are separation constants. The solutions of these equations are:

$$\begin{aligned} R(\rho) &= a_m J_\nu(k_{rm}\rho) + b_m Y_\nu(k_{rm}\rho) \\ Y(y) &= c_m e^{ik_{ym}y} + d_m e^{-ik_{ym}y} \\ \Phi(\phi) &= e^{-i\nu\phi} \end{aligned} \tag{4.9}$$

where J_ν and Y_ν are the Bessel and Neumann functions, respectively, and where $k_{rm} \equiv (k_m^2 - k_{ym}^2)^{1/2}$. The last equation in (4.9) is appropriate for a wave rotating in the positive sense. For the function to be single valued, we must choose ν to be an integer.

Equation (4.5) written out in component form becomes,

$$i\varepsilon\omega E_\rho = \frac{1}{\rho}\frac{\partial H_y}{\partial \phi} - \frac{\partial H_\phi}{\partial y}$$

$$i\varepsilon\omega E_\phi = \frac{\partial H_\rho}{\partial y} - \frac{\partial H_y}{\partial \rho} \qquad (4.10)$$

$$i\varepsilon\omega E_y = \frac{1}{\rho}\frac{\partial}{\partial \rho}(\rho H_\phi) - \frac{1}{\rho}\frac{\partial H_\rho}{\partial \phi}$$

along with three similar equations where E and H are interchanged, and where ε is replaced by $-\mu$. Since the modes of interest lie in a narrow region near the dielectric interface, we can make the approximation,

$$\frac{1}{\rho}\frac{\partial}{\partial \rho}(\rho\psi) \simeq \frac{\partial}{\partial \rho}\psi \qquad (4.11)$$

This allows us to classify the modes into two groups,[5] in each of which one of the field components is zero, and four others can be expressed in terms of the remaining component. We refer to these modes as TE and TM although strictly speaking neither one is a transverse mode. The equations which govern these modes are:

$$E_y = 0 \ (\text{TE}) \begin{cases} k_{rm}^2 E_\rho = -\mu\omega \frac{\nu}{\rho} H_y \\ k_{rm}^2 E_\phi = i\mu\omega \frac{\partial H_y}{\partial \rho} \\ k_{rm}^2 H_\phi = -i \frac{\nu}{\rho}\frac{\partial H_y}{\partial y} \\ k_{rm}^2 H_\rho = \frac{\partial^2 H_y}{\partial \rho \partial y} \end{cases} \qquad (4.12a)$$

$$H_y = 0 \quad (TM) \begin{cases} k_{rm}^2 H_\rho = \varepsilon\omega \frac{\nu}{\rho} E_y \\ k_{rm}^2 H_\phi = -i\varepsilon\omega \frac{\partial E_y}{\partial \rho} \\ k_{rm}^2 E_\phi = -i \frac{\nu}{\rho} \frac{\partial E_y}{\partial y} \\ k_{rm}^2 E_\rho = \frac{\partial^2 E_y}{\partial \rho \partial y} \end{cases} \tag{4.12b}$$

If we match boundary conditions for the solutions inside the cylinder at the boundaries marked A and B in Fig. 4.6, then, since the solutions must all have the same radial dependence, we obtain

$$k_{r1} = k_{r2} = k_{r3} \equiv k_r \tag{4.13}$$

At the boundaries A and B, we can obtain from equation (4.12) for the TE modes that the continuity of E_ρ or E_ϕ implies that H_y is continuous, and the continuity of H_ϕ or H_ρ implies that $\partial H_y/\partial y$ is continuous. Similarly for the TM modes, the continuity of H_ρ or H_ϕ implies that εE_y is continuous, and the continuity of E_ϕ and E_ρ implies that $\partial E_y/\partial y$ is continuous. Applying these continuity relations to the solutions for Y(y) in equation (4.9) allows one to solve for the dispersion relation between ω and k_r in direct analogy to the way the dispersion relation between ω and β is obtained in a planar waveguide.[8] For a restricted range of ω we can express this relationship as

$$k_r = n_{eff} \frac{\omega}{c} \tag{4.14}$$

where n_{eff} is an effective index of refraction. From the radial

dependence of the modes in equation (4.9) we see that the composite cylinder behaves as a uniform cylinder of refractive index n_{eff}.

To gain understanding of the importance of the parameter ν, we shall appeal to geometric optics. Defining a z-direction as done in Fig. 4.7, we see that the azimuthal dependence $e^{-i\nu\phi}$ can be expressed as $e^{-i(\nu/R)z}$. Thus ν/R is interpreted as the z-component of the wave vector of a ray which is bouncing about within the cylinder. From Fig. 4.7 we can see the angle of incidence of this ray to the cylinder tangent is given by

$$\sin\theta = \frac{\nu c}{R n_{eff}\omega} \tag{4.15}$$

For the ray to remain trapped within the cylinder, total internal reflection must occur, which means that we must require that

$$\nu > \frac{\omega R}{c} \tag{4.16a}$$

For modes which are tightly confined to the vicinity of the dielectric interface θ must approach 90°, and we obtain the important result

$$\nu \simeq \frac{n_{eff}\omega R}{c} \tag{4.16b}$$

An exact analytic solution to the three-layered cylinder problem does not seem possible, so a simplifying assumption will be made which is often used in analyzing dielectric waveguides.[9] The assumption is that the optical mode is sufficiently well confined to the central layer that we can disregard the continuity of the fields at the boundaries marked D and E in Fig. 4.6.

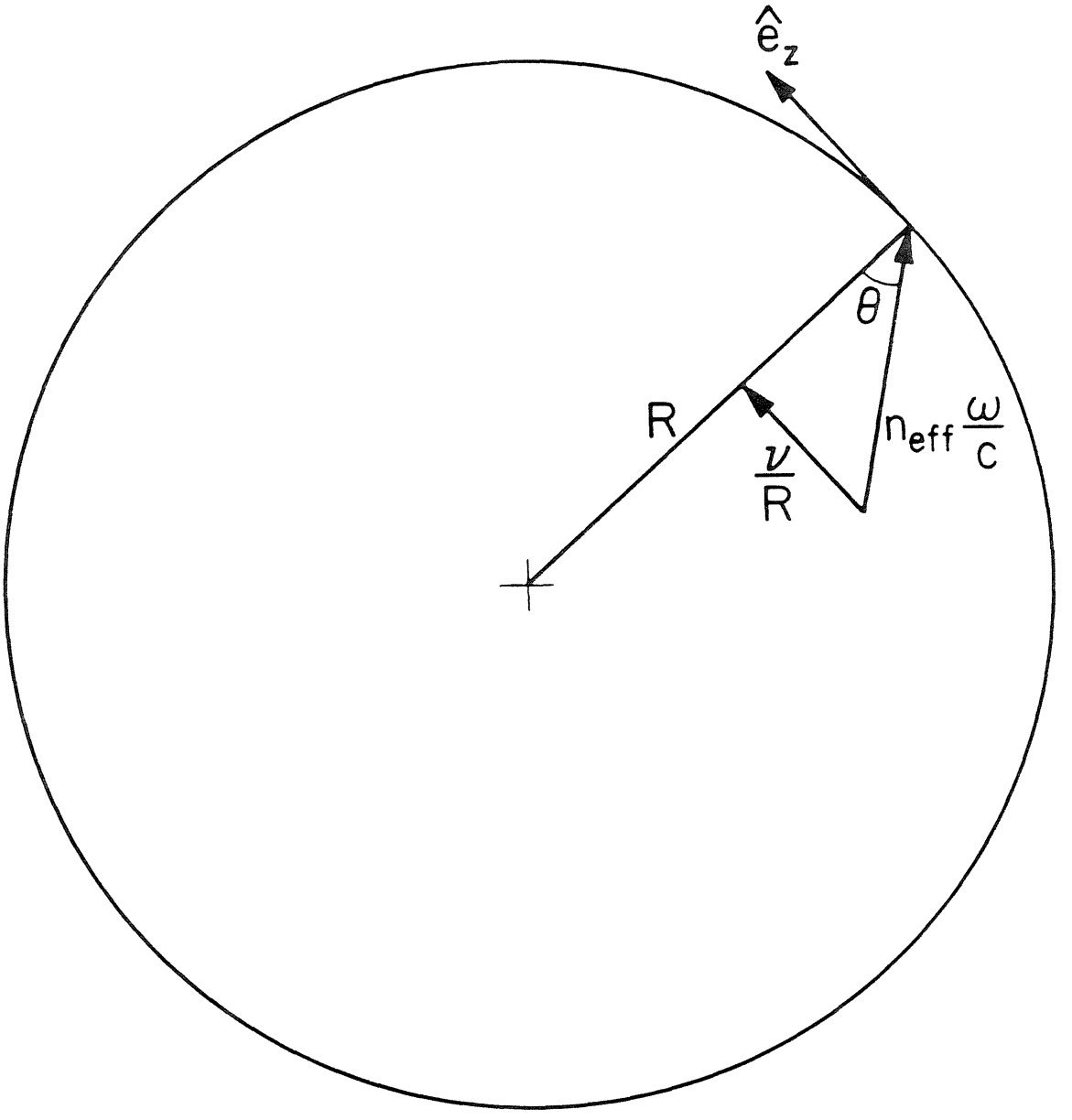

Fig. 4.7 A geometric optics interpretation of the confinement of modes in a whispering gallery laser. A mode will remain trapped in the cylinder if θ is larger than the critical angle for total internal reflection.

If we match solutions at the boundary marked C, then for the solutions to have the same y dependence we demand that $k_{y1} = k_{y0}$. The assumption of close confinement dictates that the mode should not have rapid variations in the y direction. From this it follows that $k_{y1} << k_o$, and consequently that $k_{ro} \simeq k_o$ and $k_{r2} \simeq n_2 k_o$. In this case, it also follows that $n_{eff} \simeq n_2$. To simplify the notation, in the remainder of this thesis k_o will be replaced by k, and n_2 (or n_{eff}) will be replaced by n.

At the boundary C, we can obtain from equation (4.12) for the TE modes, that the continuity of εE_ρ and E_ϕ imply that H_y and $\frac{1}{\varepsilon}\frac{\partial H_y}{\partial \rho}$ is continuous, while the fields H_ϕ and H_ρ are negligible because of our assumption that $\frac{\partial}{\partial y} << k_{ri}$. For the TM modes, the continuity of H_ϕ and H_ρ imply that E_y and $\partial E_y/\partial \rho$ are continuous. The fields E_ϕ and E_ρ are negligible using the same reasoning as above.

For a mode that is bound to the interior of the cylinder, the radial dependence of the mode, obtained from equation (4.9), is given by

$$\left\{\begin{matrix} H_y, \text{ TE} \\ E_y, \text{ TM} \end{matrix}\right\} = \begin{cases} AJ_\nu(nk\rho) & , \quad \rho < R \\ BH_\nu^{(2)}(k\rho) & , \quad \rho > R \end{cases} \tag{4.17}$$

These particular linear combinations were chosen in the interior of the cylinder because Y_ν is singular at the origin, and on the exterior because the Hankel function of the second kind represents only the physically admissible outgoing wave. Using the boundary conditions stated above, we obtain for H_y in the TE case, and for E_y in the TM case, that

$$AJ_\nu(nkR) = BH_\nu^{(2)}(kR)$$

$$AJ_\nu'(nkR) = \begin{Bmatrix} n, & \text{TE} \\ n^{-1}, & \text{TM} \end{Bmatrix} \quad BH_\nu^{(2)\prime}(kR) \tag{4.18}$$

If we divide the second equation by the first, we obtain the characteristic equation for the resonator

$$\frac{J_\nu'(nkR)}{J_\nu(nkR)} = \begin{Bmatrix} n \\ n^{-1} \end{Bmatrix} \frac{H_\nu^{(2)\prime}(kR)}{H_\nu^{(2)}(kR)} \tag{4.19}$$

where the convention which will be used in the remainder of this thesis has been made, that the upper/lower line in the braces represents TE/TM.

Solution of equation (4.19) for a given integer ν yields the resonant frequencies of the cylinder. Since $H_\nu^{(2)} = J_\nu - iY_\nu$ is in general complex, the solutions for $k = \omega/c$ will also be complex. A complex value of ω implies a finite lifetime for the mode, which is just a manifestation of the radiation loss of the curved surface. The order of the Bessel functions ν is usually a large integer, since from equation (4.16b), $\nu \simeq nkR$. The right hand side of equation (4.19) can be approximated using the following asymptotic relations,[10]

$$\begin{aligned} J_\nu(\nu \operatorname{sech} \alpha) &\sim (2\pi\nu \tanh \alpha)^{-1/2} e^{\nu(\tanh \alpha - \alpha)} \\ J_\nu'(\nu \operatorname{sech} \alpha) &\sim (4\pi\nu/\sinh 2\alpha)^{-1/2} e^{\nu(\tanh \alpha - \alpha)} \\ Y_\nu(\nu \operatorname{sech} \alpha) &\sim -(\tfrac{1}{2}\pi\nu \tanh \alpha)^{-1/2} e^{\nu(\alpha - \tanh \alpha)} \\ Y_\nu'(\nu \operatorname{sech} \alpha) &\sim (\pi\nu/\sinh 2\alpha)^{-1/2} e^{\nu(\alpha - \tanh \alpha)} \end{aligned} \tag{4.20}$$

and can be expressed as

$$\frac{H_\nu^{(2)'}(kR)}{H_\nu^{(2)}(kR)} \sim \frac{Y_\nu'(\nu/n)}{Y_\nu(\nu/n)} \sim -(n^2-1)^{1/2} \tag{4.21}$$

Using another useful asymptotic expansion for the Bessel function in terms of the Airy function[10] yields

$$J_\nu(nk\rho) \sim \left(\frac{2}{\nu}\right)^{1/3} \mathrm{Ai}\left[\left(\frac{2}{\nu}\right)^{1/3}(\nu - nk\rho)\right] \tag{4.22}$$

The characteristic equation then becomes approximately

$$\frac{\mathrm{Ai}'\left[\left(\frac{2}{\nu}\right)^{1/3}(\nu - nkR)\right]}{\mathrm{Ai}\left[\left(\frac{2}{\nu}\right)^{1/3}(\nu - nkR)\right]} = \begin{Bmatrix} n \\ n^{-1} \end{Bmatrix} (n^2-1)^{1/2} \left(\frac{\nu}{2}\right)^{1/3} \tag{4.23}$$

Since the right hand side of this equation is usually much larger than unity, an examination of the Airy function and its derivative reveals that the mode is very nearly zero at $\rho = R$. If we locate a zero of the mode at $\rho = R$, then we obtain

$$nkR = \nu - \left(\frac{\nu}{2}\right)^{1/3} |a_m| \tag{4.24}$$

where $|a_m|$ are the zeros of the Airy function, thereby confirming equation (4.16b). The width W of the m^{th} radial mode, as defined by the distance away from the interface at which the intensity has decayed to 10% of its peak value can then be given by

$$W \simeq \{(0.19) + (0.65)[m + (0.75)]^{2/3}\} \left(R\lambda^2/n^2\right)^{1/3} \tag{4.25}$$

where an approximation has been used for the zeros of the Airy function.[10] As an example, if we have $R = 100\ \mu m$, $\lambda = 0.88\ \mu m$, $n = 3.5$, and $m = 0$, then $W \simeq 1.3\ \mu m$.

We can calculate the radiation loss suffered by a mode by calculating the Poynting power carried away from the cylinder. The lifetime of the mode can be defined by

$$\tau = \frac{U_{bound}}{P_{rad}} \tag{4.25}$$

where U_{bound} is the stored energy in the mode, and P_{rad} is the power radiated away from the cylinder. Since the mode travels around the rim of the cylinder with a speed of roughly c/n, we can define an effective loss constant as

$$\alpha = \frac{n}{c\tau} \tag{4.26}$$

The amount of energy in the mode is adequately approximated by the amount of energy stored within the cylinder, which is given by

$$U_{bound} = \begin{Bmatrix} \mu \\ n^2\varepsilon_o \end{Bmatrix} \pi \int_0^R \begin{Bmatrix} |H_y|^2 \\ |E_y|^2 \end{Bmatrix} \rho d\rho \tag{4.27}$$

The radiated power can be calculated from the Poynting vector as

$$P_{rad} = 2\pi\rho \, \mathrm{Re} \begin{Bmatrix} \frac{1}{2} H_y^* E_\phi \\ -\frac{1}{2} E_y^* H_\phi \end{Bmatrix} \tag{4.28}$$

which is most easily evaluated at distances very far away from the cylinder where we can approximate

$$H_\nu^{(2)}(k\rho) \sim \left(\frac{2}{\pi k\rho}\right)^{1/2} e^{i\left(k\rho - \frac{\nu}{2} - \frac{\pi}{4}\right)} \tag{4.29}$$

Using equations (4.12), (4.16b), (4.17), (4.20), and (4.21), we obtain

after some effort,

$$\alpha = \frac{1}{R}\begin{Bmatrix} n^{-1} \\ n \end{Bmatrix}(n^2-1)^{-1/2}\ \exp\{-2\nu[\ell n(n+(n^2-1)^{1/2}) - \frac{1}{n}(n^2-1)^{1/2}]\} \tag{4.30}$$

If for example $n = 3.5$, then the quantity in square brackets is $\simeq 1$, and if, for example, $R = 100\ \mu m$ and $\lambda = 0.88\ \mu m$, then $\nu \simeq 2500$, and we conclude that the radiation loss is entirely negligible.

The observed optical loss in the curved lasers cannot be explained by radiation loss from a smooth curved surface and therefore the loss must be a result of scattering from a rough curved surface. The next section treats scattering in a general dielectric resonator, and the concluding section will apply the results to a whispering gallery laser having a rough surface.

IV.4 Mode Conversion in a Perturbed Dielectric Resonator

Dielectric resonators[11] can take on forms other than the cylinder which was described in the previous section. The objective of this section is to develop a general theoretical framework for the treatment of power loss from confined modes of a dielectric resonator whose refractive index has been perturbed. Such a perturbation can take the form of a scratch on the resonator's surface, or it can be caused by some internal flaw. The solutions to be obtained will utilize a perturbation approach which is similar to the one which has been applied to waveguides.[12]

The wave equation for the fields in the resonator, assuming that $\nabla(n_0^{-2}\ [\nabla(\Delta n^2)] \cdot \vec{\Psi})$ is "small," is given by

$$\nabla^2\vec{\Psi} = \left(\frac{n_o^2 + \Delta n^2}{c^2}\right) \frac{\partial^2\vec{\Psi}}{\partial t^2} \tag{4.31}$$

where Δn^2 represents the influence of the perturbation. The resonator will be imagined to have sufficient optical gain, not necessarily uniformly distributed in space, such that there exists one mode which is lasing, i.e., a mode whose lifetime is infinite. In addition, there will be a spectrum of quasi-bound (QB) modes that are confined to the resonator by total internal reflection, and there will also be a spectrum of unconfined radiation modes. Assuming an $e^{i\omega t}$ dependence, the unperturbed fields obey the following time-independent wave equations,

$$\begin{aligned}
&\text{Lasing Mode:} && \nabla^2\vec{\psi}_o + \frac{n_o^2}{c^2}\omega_o^2\vec{\psi}_o = 0 \\
&\text{QB Modes:} && \nabla^2\vec{\psi}_\ell + \frac{n_o^2}{c^2}(\omega_\ell^2 + i\omega_\ell/\tau_\ell)\vec{\psi}_\ell = 0 \\
&\text{Radiation Modes:} && \nabla^2\vec{\psi}_{m\omega} + \frac{n_o^2}{c^2}\omega^2\vec{\psi}_{m\omega} = 0
\end{aligned} \tag{4.32}$$

where ω_o is the lasing frequency, and where ω_ℓ and τ_ℓ are the resonant frequencies and lifetimes respectively of the QB modes. The above separation of the modes is highly useful, although somewhat artificial, because all the modes, since they do radiate, can be described by a superposition of radiation modes. The lasing mode can be thought of as a QB mode with τ infinite. The modes are normalized to energy U, where for the QB modes and the lasing mode it is understood that the radiation field is to be disregarded. The orthogonality of the lasing and QB mode electric fields is given by

$$\int \frac{1}{2} \varepsilon_o n_o^2 \vec{\psi}_\mu^* \cdot \vec{\psi}_\lambda d^3r = U\delta_{\mu\lambda} \tag{4.33}$$

and for the radiation modes we have

$$\int \frac{1}{2} \varepsilon_o n_o^2 \vec{\psi}_{\mu\omega}^* \cdot \vec{\psi}_{\lambda\omega} d^3r = U\delta_{\mu\lambda} \delta(\omega-\omega') \tag{4.34}$$

where delta function normalization has been applied. If magnetic rather than electric fields are used, then ε_o is to be replaced by $\mu/\bar{n}^2$ in equations (4.33) and (4.34), where $\bar{n}$ is an averaged index of refraction (see the appendix).

Let us consider a time-dependent superposition of modes whose coefficients are slowly varying

$$\vec{\Psi}(t) = C_o(t) \vec{\psi}_o e^{i\omega_o t} + \sum_j C_j(t) \vec{\psi}_j e^{i\omega_j t} + \sum_k \int_{-\infty}^{\infty} d\omega g_k(\omega;t) \vec{\psi}_{k\omega} e^{i\omega t} \tag{4.35}$$

If this is inserted into equation (4.31), equation (4.32) can be used to cancel some of the terms, to yield

$$\begin{aligned}
&(\ddot{C}_o + 2i\omega_o \dot{C}_o) \vec{\psi}_o e^{i\omega_o t} \\
&\quad + \sum_j (\ddot{C}_j + 2i\omega_j \dot{C}_j + i(\omega_j/\tau_j) C_j) \vec{\psi}_j e^{i\omega_j t} \\
&\quad + \sum_k \int_{-\infty}^{\infty} d\omega (\ddot{g}_k + 2i\omega \dot{g}_k) \vec{\psi}_{k\omega} e^{i\omega t} \\
&= -\Delta n^2/n_o^2 [(\ddot{C}_o + 2i\omega_o \dot{C}_o - \omega_o^2 C_o) \vec{\psi}_o e^{i\omega_o t} + \sum_j (\ddot{C}_j + 2i\omega_j \dot{C}_j - \omega_j^2 C_j) \vec{\psi}_j e^{i\omega_j t} \\
&\quad + \sum_k \int_{-\infty}^{\infty} d\omega (\ddot{g}_k + 2i\omega \dot{g}_k - \omega^2 g_k) \vec{\psi}_{k\omega} e^{i\omega t}]
\end{aligned} \tag{4.36}$$

Equation (4.36) can be used to determine the effect the perturbation has on coupling power out of the lasing mode and into QB and radiation modes. Let us begin with a discussion of coupling into the quasi-bound modes. If equation (4.36) is scalar multiplied by $\frac{1}{2}\varepsilon \vec{\psi}_\ell^* e^{-i\omega_\ell t}$ and integrated over all space, then retaining only first order terms and using equation (4.33) yields

$$2i\omega_\ell \dot{C}_\ell + i(\omega_\ell/\tau_\ell)C_\ell = U^{-1}\omega_o^2 C_o M_{\ell o} e^{i(\omega_o-\omega_\ell)t} \tag{4.37}$$

where the matrix element $M_{\ell o}$ which connects the lasing mode and a QB mode is given by

$$M_{\ell o} = \int \frac{1}{2} \varepsilon_o \Delta n^2 \vec{\psi}_\ell^* \cdot \vec{\psi}_o \, d^3r \tag{4.38}$$

Assuming that the perturbation has been operating for an infinite time, the solution to equation (4.37) assuming C_o constant becomes,

$$|C_\ell|^2 = \left|\frac{1}{2U}\frac{\omega_o^2}{\omega_\ell} M_{\ell o}\right|^2 |C_o|^2 [(\omega_o-\omega_\ell)^2 + (1/2\tau_\ell)^2]^{-1} \tag{4.39}$$

The energy stored in a mode is given by $|C_\ell|^2 U$. We shall take $|C_o|^2 = 1$. Since energy is constantly being lost from the QB mode through radiation, its energy must be resupplied by coupling from the lasing mode. In steady state we can heuristically write

$$0 = \frac{d}{dt}|C_\ell|^2 U = P_{o\to\ell} - \frac{|C_\ell|^2 U}{\tau_\ell} \tag{4.40}$$

where $P_{o\to\ell}$ is the power transferred from the lasing mode to the ℓ^{th} QB mode. The total power lost by the lasing mode can then be given by

$$P_{0\to} = \sum_{\ell} P_{0\to\ell} = \int \rho(\omega_\ell)\, P_{0\to\ell}\, d\omega_\ell \tag{4.41}$$

where $\rho(\omega_\ell)$ is the density of QB states. We can solve for $P_{0\to\ell}$ from equations (4.40) and (4.41), from which we conclude that $P_{0\to\ell}$ is large only in the vicinity of $\omega_\ell = \omega_o$. Performing the integration indicated in equation (4.41), assuming that ρ and $M_{0\ell}$ do not vary rapidly, whereby $M_{\ell 0}$ can be replaced by a constant M_{f0}, leads to a "golden rule,"

$$P_{0\to} = \frac{\pi}{2U}\, \omega_o^2 |M_{f0}|^2\, \rho(\omega_o) \tag{4.42}$$

If there are other "quantum numbers" which shall be denoted by q in the final states, then we must sum over all these contributions, and we obtain from equation (4.25)

$$\tau_{QB}^{-1} = U^{-1} \sum_{q} P_{0\to q}$$

$$= \sum_{q} \frac{\pi}{2U^2}\, \omega_o^2\, |M_{qo}|^2\, \rho_q(\omega_o) \tag{4.43}$$

This is our final result for τ_{QB}, the power loss rate constant for power transfer from the lasing mode to the QB modes.

To determine the loss in the lasing mode due to coupling into the radiation modes, we can scalar multiply equation (4.36) by $\frac{1}{2}\varepsilon \vec{\psi}^*_{m\omega'}\, e^{-i\omega' t}$ and integrate over all space, then retaining only first order terms, and using equation (4.34) yields,

$$\dot{g}_m = -\frac{i}{2U}\, \frac{\omega_o^2}{\omega}\, M_{mo}\, e^{i(\omega_o-\omega)t}\, C_o \tag{4.44}$$

where the matrix element M_{mo} is given by

$$M_{mo} = \int \frac{1}{2} \varepsilon_o \Delta n^2 \vec{\psi}_m^* \cdot \vec{\psi}_o \, d^3r \tag{4.45}$$

If equation (4.44) is integrated from t = -T/2 to t = T/2, we obtain

$$g_m = - \frac{1}{U} \frac{\omega_o^2}{\omega} C_o M_{mo} \frac{\sin(\omega_o-\omega)T/2}{\omega_o-\omega} \tag{4.46}$$

from which it can be seen that g_m is peaked near $\omega = \omega_o$. Since the energy in a radiation mode is given by

$$U_m = U \int_{-\infty}^{\infty} |g_m|^2 \, d\omega \tag{4.47}$$

it follows, assuming g_m and M_{mo} do not vary rapidly, that

$$U_m = \frac{\pi}{2U} \omega_o^2 |C_o|^2 \, |M_{mo}|^2 \, T \tag{4.48}$$

The power transferred into radiation mode m is then just U_m/T. From equation (4.25) we can obtain the power loss rate constant for power transfer from the lasing mode to the radiation modes to be

$$\tau_{rad}^{-1} = U^{-1} \sum_m P_{0 \to m}$$

$$= \sum_m \frac{\pi}{2U^2} \omega_o^2 \, |M_{mo}|^2$$

IV.5 Scattering Loss in Whispering Gallery Lasers

In this section, equations (4.43) and (4.49) will be applied to the case of the whispering gallery laser which will be modeled as in Section IV.3. The perturbation which causes the scattering in the whispering

gallery laser is the roughness of the dielectric interface. The roughness will be modeled by vertical scratches on the composite dielectric cylinder of Fig. 4.6. The dielectric interface is located at $\rho = R + f(\phi)$, where $f(\phi)$ is a random variable. The square of the index perturbation is given by

$$\Delta n^2 = \begin{cases} \left\{ \begin{array}{lll} 0 & , & \rho < R+f \\ -(n^2-1) & , & R+f < \rho < R \\ 0 & , & \rho > R \end{array} \right\} & f < 0 \\ \left\{ \begin{array}{lll} 0 & , & \rho < R \\ (n^2-1) & , & R < \rho < R+f \\ 0 & , & \rho > R+f \end{array} \right\} & f > 0 \end{cases} \tag{4.50}$$

Let us first consider scattering into the nonlasing quasi-bound modes. The spatial dependence of the lasing mode, neglecting the y-dependence, is given by

$$\psi_\nu = AJ_\nu(nk\rho)e^{-i\nu\phi} \qquad \rho \leq R \tag{4.51}$$

while the QB modes are described by

$$\psi_{\nu'\ell} = EJ_{\nu'}(nk\rho)e^{-i\nu'\phi} \qquad \rho \leq R \tag{4.52}$$

If we take the surface roughness to be very small, then the matrix element defined by equation (4.38) becomes

$$M_{\nu'\nu} = \pi R \left\{ \begin{matrix} n^{-2} \\ \varepsilon_o \end{matrix} \right\} (n^2-1)\, E\, J_{\nu'}(nkR)\, A\, J_\nu(nkR)\; I_{\nu'\nu} \tag{4.53}$$

where the upper/lower line in the braces corresponds to TE/TM, and where

$$I_{\nu'\nu} \equiv \int_{-\pi R}^{\pi R} f(\phi)\, e^{-i(\nu-\nu')\phi}\, d\phi \tag{4.54}$$

which defines a term in a Fourier series for $f(\phi)$. If we define a wall distortion function $p(z) = f(z/R)$, where the z-direction is as defined in Fig. 4.7, the wall distortion function can be expanded into a Fourier series as

$$p(z) = \sum_{\nu'} I_{\nu'\nu}\, e^{i(\nu-\nu')z/R} \tag{4.55}$$

We may characterize $p(z)$ in terms of a correlation function

$$\xi(x) = \langle p(z)\, p(z+x) \rangle \tag{4.56}$$

whereby it becomes fairly easy to show that

$$|I_{\nu'\nu}|^2 = \frac{1}{\pi R} \int_0^{\pi R} \xi(x)\, \cos((\nu-\nu')x/R)\, dx \tag{4.57}$$

We shall choose a particular form for the correlation function, viz.,

$$\xi(x) = H^2\, e^{-|x|/B} \tag{4.58}$$

where H is the r.m.s. amplitude of the wall distortion function and B is its correlation length. From this we obtain

$$|I_{\nu'\nu}|^2 = \frac{H^2}{2kR}\, P_{\nu'} \tag{4.59}$$

where

$$P_{\nu'} \equiv (2/\pi)Bk\, \{1 + [Bk(\nu-\nu')/kR]^2\}^{-1} \tag{4.60}$$

The mode normalization constants can be found in a straightforward manner to be given by

$$\frac{1}{2}\left\{\begin{matrix}\mu\\ n^2\varepsilon_o\end{matrix}\right\}A^2 = \frac{1}{\pi R^2}\, U[J'_\nu(nkR)]^{-2}$$

$$\frac{1}{2}\left\{\begin{matrix}\mu\\ n^2\varepsilon_o\end{matrix}\right\}E^2 = \frac{1}{\pi R^2}\, U\,[J'_{\nu'}(nkR)]^2 + [1 - (\frac{\nu'}{nkR})^2][J_{\nu'}(nkR)]^{2\ -1} \qquad (4.61)$$

From the characteristic equation (4.19) and the asymptotic expansions in equation (4.20) we find

$$[J'_{\nu'}(nkR)/J_{\nu'}(nkR)] = \left\{\begin{matrix}n\\ n-1\end{matrix}\right\}[(\frac{\nu'}{k\rho})^2 - 1]^{1/2} \qquad (4.62)$$

In order to find the density of QB states we appeal again to equation (4.20), and considering the argument of the cosine in the expansion of the Bessel function, we can write for a group of modes near $\omega = \omega_o$ that,

$$\nu'\{[(\frac{nkR}{\nu'})^2 - 1]^{1/2} - \sec^{-1}(\frac{nkR}{\nu'})\} = (q+a)\pi \qquad (4.63)$$

where q is an integer, and a is some constant. It then follows that

$$\rho_{\nu'}(\omega) = \frac{dq}{d\omega}$$

$$= \frac{nR}{\pi c}[1 - (\frac{\nu'}{nkR})^2]^{1/2} \qquad (4.64)$$

If we now combine equations (4.26), (4.43), and the equations derived in this section, we obtain finally

$$\alpha_{QB} = \frac{kH^2}{R^2}\sum_{\nu'} Q_{\nu'}P_{\nu'}$$

$$\rightarrow \frac{k^2H^2}{R}\int Q_{\nu'}(\frac{\nu'}{kR})\ P_{\nu'}(\frac{\nu'}{kR})\ d(\frac{\nu'}{kR}) \qquad (4.65)$$

where the limit has been taken into the continuum, and where the "coupling strength" is given by

$$Q_{\nu'} = \frac{(\frac{n^2-1}{n^2})\begin{Bmatrix} n^{-2} \\ n^2 \end{Bmatrix}[1 - (\frac{\nu'}{nkR})^2]^{1/2}}{[(\frac{\nu'}{kR})^2 - 1]\begin{Bmatrix} n^2 \\ n^{-2} \end{Bmatrix} + [1 - (\frac{\nu'}{nkR})^2]}$$

The second contribution to the loss comes from scattering to the radiation modes. To describe the radiation modes, we imagine performing an experiment in which we illuminate the cylinder, and examine the field that is built up in the resonator and the field that is reflected from the cylinder. Since the interior of a whispering gallery laser is highly absorbing, we can approximate the field inside the resonator as being composed of only an inwardly travelling wave. The mode is written as

$$\psi_{\nu'\omega} = \begin{cases} C\, H_{\nu'}^{(1)}(nk\rho)\ e^{-i\nu'\phi}, & \rho < R \\ D\, H_{\nu}^{(1)}(k\rho) + F\, H_{\nu}^{(2)}(k\rho)\ e^{-i\nu'\phi}, & \rho > R \end{cases} \tag{4.67}$$

The matrix element given by equation (4.45) becomes

$$|M_{\nu'\nu}|^2 = \begin{Bmatrix} \mu^2 \\ \varepsilon_o^2 \end{Bmatrix} (\pi R)^2\ (n^2-1)^2\ |C|^2\ |H_{\nu'}^{(1)}(nkR)|^2 |A|^2 \times |J_{\nu}(nkR)|^2\ |I_{\nu'\nu}| \tag{4.68}$$

The calculation required to determine the normalization constant C is extremely lengthy and will only be outlined here.

The constants D and F in the combination $|D|^2 + |F|^2$ can be determined from the normalization condition (4.34) by expressing the Hankel

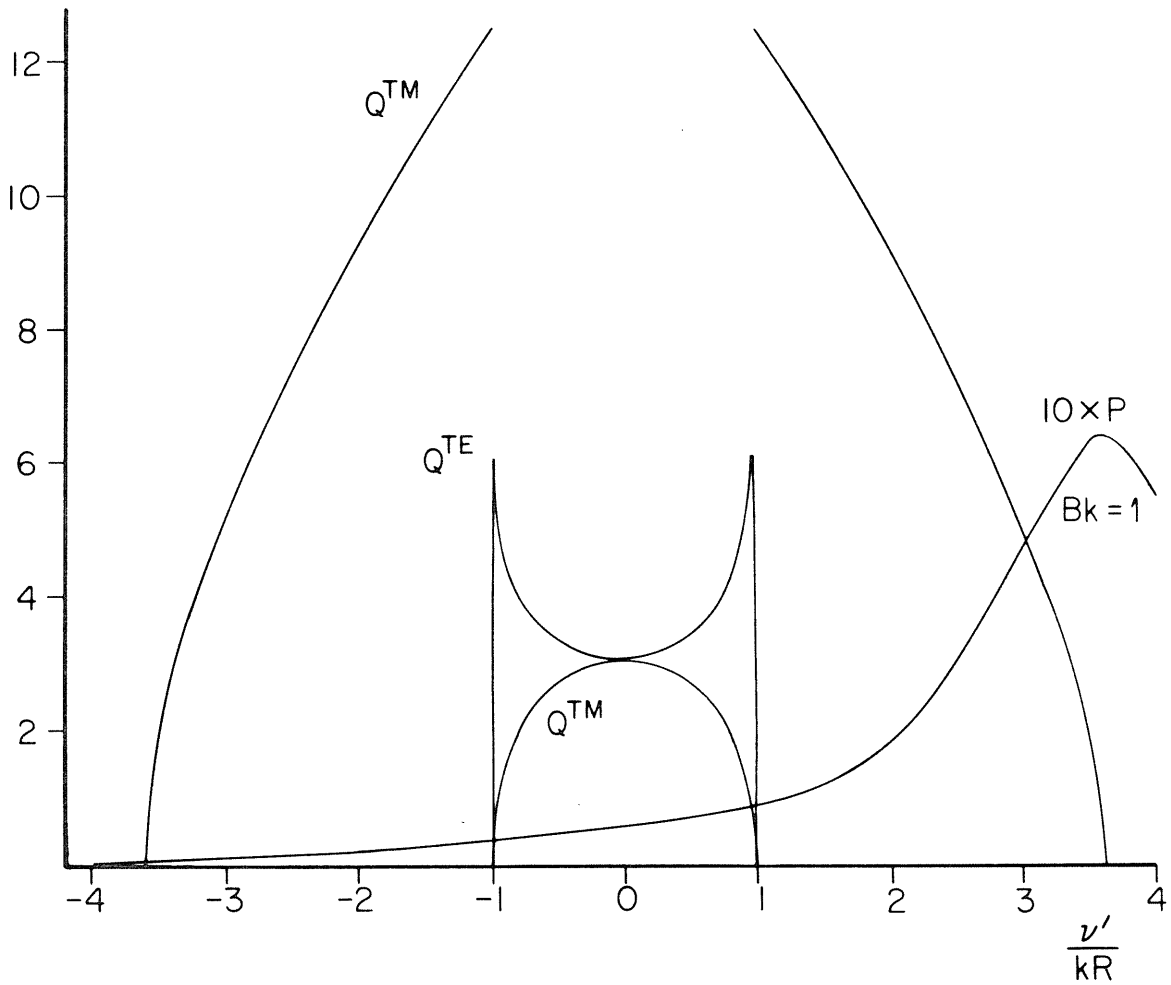

Fig. 4.8 A plot of the coupling strengths Q for TE and TM modes. The range $|\nu'/kR| < 1$ corresponds to radiation modes, while the range $1 < |\nu'/kR| < 3.6$ corresponds to bound modes. Also shown is an example of P, the power spectrum of the wall distortion function.

functions in their asymptotic form for very large distances to yield

$$\frac{1}{2}\left\{\begin{matrix}\mu\\ \varepsilon_o\end{matrix}\right\}(|D|^2 + |F|^2) = \frac{\omega}{4\pi c^2} U \tag{4.69}$$

From the boundary conditions at the dielectric interface we have,

$$CH^{(1)}_{\nu'}(nkR) = D\, H^{(1)}_{\nu'}(kR) + F\, H^{(2)}_{\nu'}(kR)$$

and

$$CH^{(1)'}_{\nu'}(nkR) = \left\{\begin{matrix}n\\ n^{-1}\end{matrix}\right\}[D\, H^{(1)'}_{\nu'}(kR) + F\, H^{(2)'}_{\nu'}(kR)] \tag{4.70}$$

from which we can express $|C|^2$ in terms of $|D|^2 + |F|^2$. After applying equations (4.20) to the Hankel functions, we obtain after some labor

$$\alpha_{rad} = \frac{H^2 k}{R^2} \sum_{\nu'} Q_{\nu'}\, P_{\nu'}$$

$$\rightarrow \frac{H^2 k^2}{R} \int Q_{\nu'}(\tfrac{\nu'}{kR})\, P_{\nu}(\tfrac{\nu'}{kR})\, d(\tfrac{\nu'}{kR}) \tag{4.71}$$

where the coupling strength is given by

$$Q_{\nu'} = \frac{\left\{\begin{matrix}n^{-1}\\ n\end{matrix}\right\}\, n^2 - 1}{[1 - (\tfrac{\nu'}{kR})^2]^{1/2} + \left\{\begin{matrix}n^{-2}\\ n^2\end{matrix}\right\}[1 - (\tfrac{\nu'}{nkR})^2][1 - (\tfrac{\nu'}{kR})^2]^{-1/2}} \tag{4.72}$$

The coupling strengths Q for the quasi-bound modes, equation (4.66) and for the radiation modes, equation (4.72) are plotted in Fig. 4.8 for n = 3.6. The range $|\nu'| > kR$ corresponds to quasi-bound modes (see the discussion surrounding equation (4.15)), while

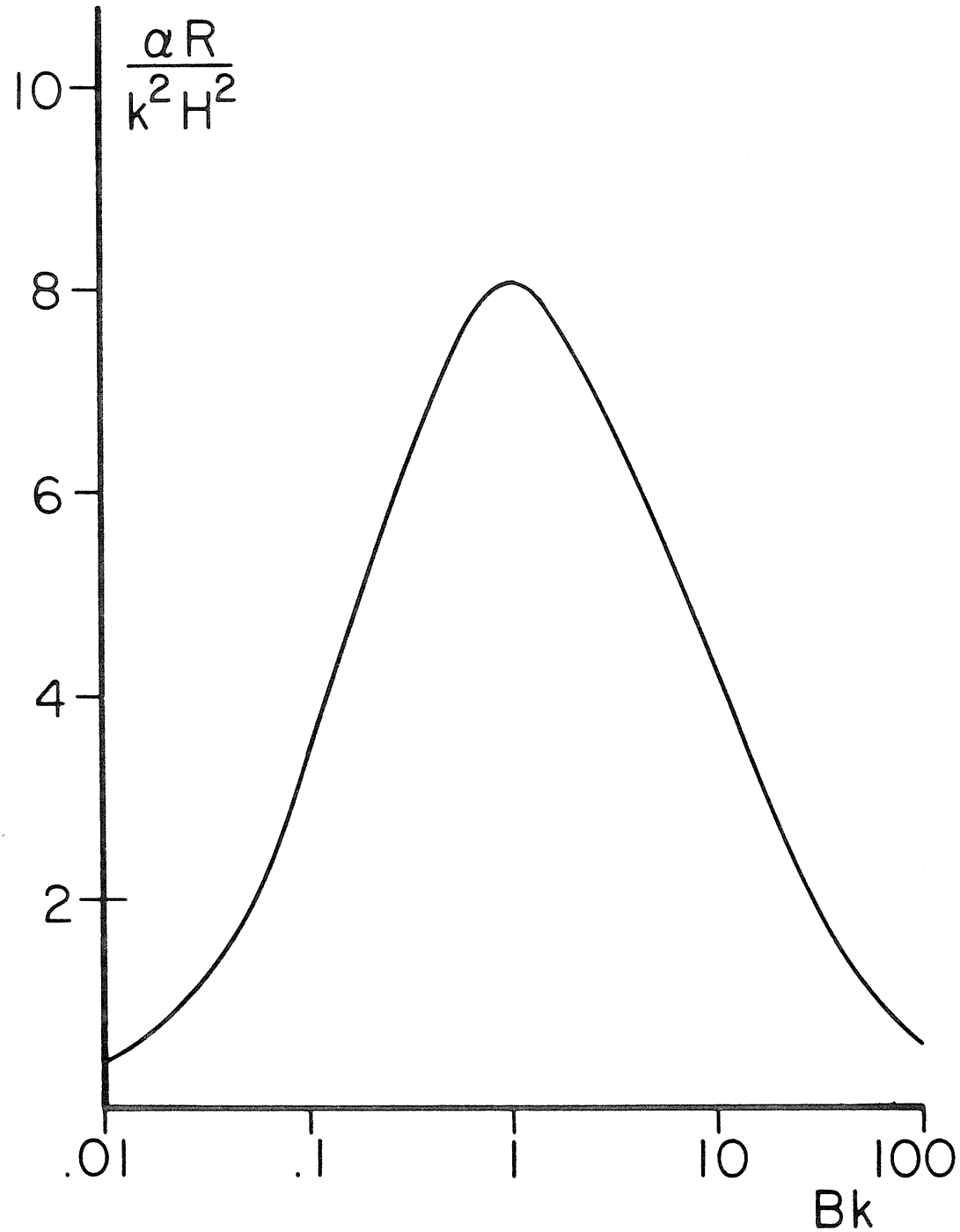

Fig. 4.9 Optical loss constant for the TM lasing mode of a whispering gallery laser versus the correlation length of the wall distortion function.

$|\nu'| < kR$ corresponds to radiation modes. The positive ν' represent forward rotating waves while the negative ν' represent backward rotating waves. As can be seen in the figure, for a TM mode the loss to QB modes dominates, while for a TE mode loss to radiation modes dominates. The total loss obtained by taking the overlap integral of Q and P for a TM wave is plotted in Fig. 4.9 as a function of the correlation length B of the wall distortion function.

The suppression of the coupling between QB TE modes is due to the fact that these modes almost vanish at the interface. The above analysis has been carried out for very small perturbations. In the case of larger perturbations, it seems reasonable that the coupling between QB TE modes can become appreciable. For the curved lasers described in Section IV.2 the emission was equally polarized TE and TM, although the straight control lasers were strongly polarized TE. This indicates that the loss for one of the polarizations was not substantially larger than for the other. It is to be noted that the 1/R dependence for the loss shown in Fig. 4.5 is predicted in equations (4.65) and (4.72). Using the peak of the loss in Fig. 4.9, the observed loss in Fig. 4.5 can be explained by an r.m.s. roughness of 0.1 μm.

REFERENCES FOR CHAPTER IV

1. H. C. Casey and M. B. Panish, Heterostructure Lasers: Part B, Materials and Operating Characteristics, Academic Press, New York (1978).

2. J. L. Merz and R. A. Logan, "GaAs Double Heterostructure Lasers Fabricated by Wet Chemical Etching," J. Appl. Phys. 47, 3503 (1976).

3. W. Ng, H. W. Yen, A. Katzir, I. Samid, and A. Yariv, "Room-Temperature Operation of GaAs Bragg-Mirror Lasers," Appl. Phys. Lett. 29, 684 (1976).

4. Lord Rayleigh, Scientific Papers, Vol. 5, Cambridge University, Cambridge, England (1912).

5. E.A.J. Marcatili, "Bend in Optical Dielectric Guides," Bell System Tech. J. 48, 2103 (1969).

6. N. Matsumoto and K. Kumabe, "AlGaAs-GaAs Semiconductor Ring Laser," Jap. J. Appl. Phys. 16, 1395 (1977).

7. F. Stern, "Calculated Spectral Dependence of Gain in Excited GaAs," J. Appl. Phys. 47, 5382 (1976).

8. A. Yariv, Introduction to Optical Electronics, 2nd edition, Holt, Rinehart, and Winston, New York (1976).

9. E.A.J. Marcatili, "Dielectric Rectangular Waveguide and Directional Coupler for Integrated Optics," Bell Syst. Tech. J. 48, 2071 (1969).

10. M. Abramowitz and I. A. Stegun, Handbook of Mathematical Functions, National Bureau of Standards, Washington, D.C. (1972).

11. R. D. Richtmeyer, "Dielectric Resonators," J. Appl. Phys. 10, 391 (1939).

12. D. Marcuse, "Mode Conversion Caused by Surface Imperfections of a Dielectric Slab Waveguide," Bell System Tech. J. 48, 3187 (1969).

Appendix

Mode Normalization in a Dielectric Resonator

Consider one of the vector components of equation (4.32) which we write as

$$\nabla^2\psi + \frac{\omega^2}{c^2} n^2\psi = 0 \tag{A.1}$$

where ψ is a field component of either a lasing mode, a Q-B mode, or a radiation mode, n is the spatially dependent, possibly complex, refractive index, and where ω is the possibly complex, resonant frequency. We will first show how these modes can be normalized in terms of their energy. This will be followed by a proof of the orthogonality of the modes.

If we multiply equation (A.1) by ψ^* and use a property of the ∇ operator we obtain

$$\nabla\cdot(\psi^*\nabla\psi) - \nabla\psi^*\cdot\nabla\psi + \frac{\omega^2}{c^2} n^2\psi^*\psi = 0 \tag{A.2}$$

If equation (A.2) is integrated over a volume, and Green's theorem is applied, we get

$$\int (\psi^*\nabla\psi)\cdot dS - \int \nabla\psi^*\cdot\nabla\psi \, d\,vol + \frac{\omega^2}{c^2}\int n^2\psi^*\psi \, d\,vol = 0 \tag{A.3}$$

If the surface of the volume chosen is far away from the resonator, then the first integral in equation (A.3) can be neglected for the following reason. For the lasing and Q-B modes the fields are taken to vanish far away from the resonator and so the integral also vanishes. For the radiation modes, where delta function normalization is applied, the integral over the surface will be vanishingly small compared to the integral over the volume.

Since the second integral in equation (A.3) is evidently real, it follows that $\omega^2 \int n^2 \psi^* \psi \, dvol$ is also real. If ψ represents a component of the electric field, then we know that the stored electric energy for n real is given by

$$U_{electric} = \frac{1}{4} \int \varepsilon_o n^2 \vec{\psi}^* \cdot \vec{\psi} \, dvol \tag{A.4}$$

In a time-harmonic electromagnetic field, the average energy stored in the electric field is equal to that stored in the magnetic field, from which we obtain

$$U = 2U_{electric} = 2U_{magnetic} \tag{A.5}$$

where U is the total stored energy. If the imaginary part of the refractive index is negligibly small, then by combining equations (A.4) and (A.5) we obtain

$$\int n^2 \vec{\psi}^* \cdot \vec{\psi} \, dvol = 2U/\varepsilon_o \tag{A.6}$$

If ψ represents a component of the magnetic field, then we know that the stored magnetic energy is given by

$$U_{magnetic} = \frac{1}{4} \int \mu \vec{\psi}^* \cdot \vec{\psi} \, dvol \tag{A.7}$$

It then follows that,

$$\int n^2 \vec{\psi}^* \cdot \vec{\psi} \, dvol = 2\bar{n}^2 U / \mu \tag{A.8}$$

where $\bar{n}$ is an averaged refractive index given by

$$\bar{n}^2 = \frac{\int n^2 \vec{\psi} \cdot \vec{\psi} \, dvol}{\int \vec{\psi}^* \cdot \vec{\psi} \, dvol} \tag{A.9}$$

In equation (4.53) for the Q-B modes we will take $\bar{n} \simeq n$, since the modes are tightly confined to the cylinder, while in equation (4.68) for the radiation modes we will take $\bar{n} \simeq 1$, since the modes exist essentially in free space.

To prove that the modes are orthogonal, consider two modes whose wave equations are

$$\begin{aligned} \nabla^2\psi_1 + \frac{\omega_1^2}{c^2} n^2\psi_1 &= 0 \\ \nabla^2\psi_2 + \frac{\omega_2^2}{c^2} n^2\psi_2 &= 0 \end{aligned} \tag{A.10}$$

If we multiply the first equation by ψ_2^* and subtract from it the product of ψ_1 and the complex conjugate of the second equation and integrate, we obtain

$$\int (\psi_2^*\nabla\psi_1 - \psi_1\nabla\psi_2^*)\cdot dS = \left(\frac{\omega_2^*}{c}\right)^2 \int n^{*2} \psi_2^*\psi_1 \, d\,vol - \left(\frac{\omega_1}{c}\right)^2 \int n^2\psi_2^*\psi_1 \, d\,vol \tag{A.11}$$

The left hand side of the equation vanishes for reasons already given. Barring any accidental degeneracies, the right hand side of the equation vanishes only if $\psi_1 = \psi_2$ for which both terms on the right hand side are real as has been already shown. The statement of orthogonality is given by equation (4.34).